

Advances in Nano-Optics and Nano-Photonics

'Tip Enhancement'

Edited by S. Kawata and V.M. Shalaev

2007

Elsevier Science

Chapter 10 (pg. 115-155)

Use of tip-enhanced vibrational spectroscopy for analytical applications in chemistry, biology, and materials science

Thomas Schmid, Boon-Siang Yeo, Weihua Zhang, and Renato Zenobi*

Department of Chemistry and Applied Biosciences,

ETH Zurich,

8093 Zurich, Switzerland.

*correspondence to R. Zenobi

phone: +41 44 632 4376

fax: +41 44 632 1292

e-mail: zenobi@org.chem.ethz.ch

Keywords: tip-enhanced Raman spectroscopy (TERS), coherent anti-Stokes Raman scattering (CARS), scattering scanning near-field optical microscopy (s-SNOM), tip fabrication, enhancement factor, contrast, lateral resolution, dyes, catalysis, biopolymers, adenine, DNA, biological tissues, viruses, insects, single-walled carbon nanotubes (SWNT), material-specific mapping, semiconductors, SERS substrates

1. Introduction

Proposed as early as 1985 (Wessel 1985), the combination of optical field confinement by a metallic tip with vibrational spectroscopy has opened a way for molecular analysis and identification with true nanoscale spatial resolution. Three different principles to achieve this have appeared in the literature:

- Raman Spectroscopy: by dispersing inelastically scattered photons, usually from Stokes scattering, in a spectrometer. Due to its similarity to surface-enhanced Raman spectroscopy (SERS), the apertureless near-field version is commonly referred to as tip-enhanced Raman spectroscopy (TERS). It can be performed at irradiation wavelengths in the visible or the near IR.
- Coherent anti-Stokes Raman scattering (CARS): CARS is a nonlinear optical spectroscopic method based on four-wave mixing. It requires two synchronized tunable lasers and has advantages because it eliminates much of the background inherent in the other two methods. However, it is technically more difficult to implement, which is evident from the relative paucity of literature employing a CARS set-up.
- IR (scattering) spectroscopy: by detecting a contrast in the scattering efficiency as a function of wavelength. This arrangement is usually called scattering scanning near-field optical microscopy (s-SNOM). It requires infrared (IR) light, preferably in the form of a tunable IR laser, for excitation of the sample.

In this chapter we will discuss the experimental set-up for implementing TERS, tip-enhanced CARS, and s-SNOM. We will then focus on the heart of such experiments, the tip, describe tip fabrication methods, and discuss enhancement factors, contrast, and spatial resolution in detail. This is then followed by a thorough review of the literature on applications in the fields of organic molecules, catalysis, biology, nanotubes, and semiconductors.

2. Setups for Tip-enhanced Vibrational Spectroscopy

2.1. Tip-enhanced Raman Spectroscopy (TERS)

The key point of TERS is to create a strong and localized light source using a sharp metal tip. Classical electromagnetic theory predicts that the incident field will be enhanced greatly at the end of the tip at resonance because of the excitation of localized plasma polaritons (Zayats 1999). There are two different types of localized plasma polaritons which are used in TERS. One is referred to as the “lightning rod” effect. It suggests that when an isolated sharp metal tip is illuminated, the p component of the field will be greatly enhanced at resonance (Novotny, Bian and Xie 1997). Another method is using the “gap mode” of the electromagnetic field (Aravind and Metiu 1983). In theory, the p component of the electromagnetic field at a tip-substrate junction can be enhanced more than 100 times under the resonant condition of the gap mode. With this method, a 10^6 times enhancement of Raman signal intensity was achieved recently (Pettinger, Ren, Picardi, Schuster and Ertl 2004). It should be mentioned that besides these two methods, isolated noble metal nanoparticles can also enhance the electric field efficiently. For example, a single gold nanoparticle has been attached to the apex of a fiber tip for a similar purpose (Kalkbrenner, Ramstein, Mlynek and Sandoghdar 2001), but to date, there is no reports utilizing such probes for TERS.

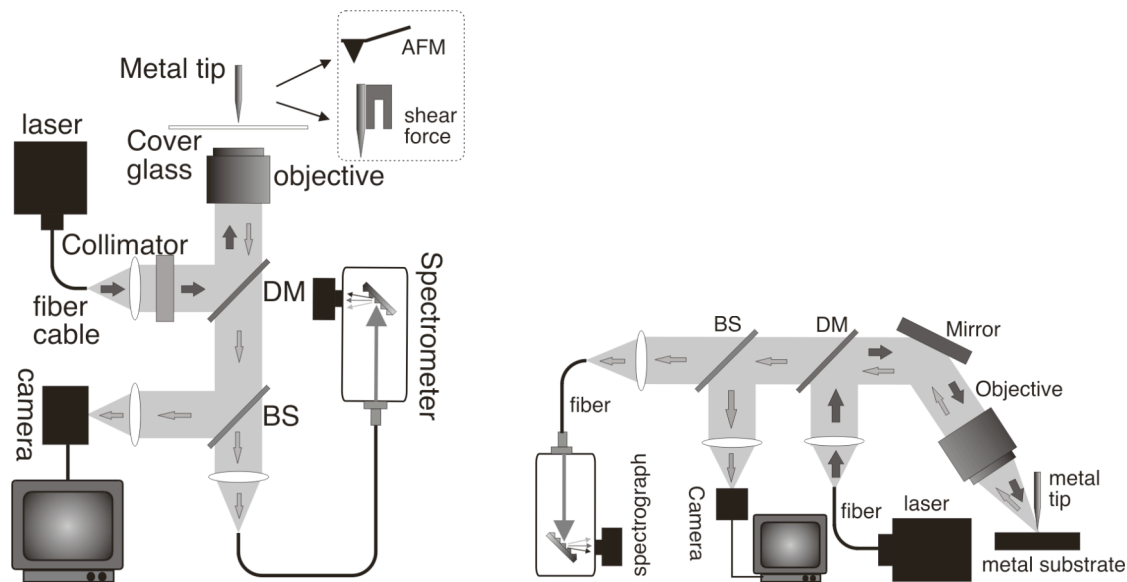


Fig. 1: Illumination and detection schemes in tip-enhanced vibrational spectroscopy. The left figure is the transmission mode. The right figure is the side illumination mode. DM: dichroic mirror, BS: beam splitter.

For TERS based on the “lightning rod” effect, epi-illumination (transmission mode) is popular (Fig. 1), because a large numerical aperture (NA) microscope objective can be used to afford a tight focus. This is crucial for decreasing the background noise induced by far-field illumination. There are two disadvantages of this type of transmission-illumination setup. First, a transparent sample is necessary. Second, this setup is not efficient for creating a p-polarized component from a linearly polarized illumination beam. To overcome this problem, different solutions have been adopted, annular illumination (Hayazawa, Inouye, Sekkat and Kawata 2000) or modifying the wave front using a wave plate (Novotny, Sanchez and Xie 1998, Saito, Hayazawa, Kataura, Murakami, Tsukagoshi, Inouye and Kawata 2005). It should be mentioned that no matter which method is chosen to create a p component for the illumination, a high NA objective is required.

For gap mode TERS, side illumination scheme is normally employed, because an opaque metal substrate is used (Fig. 1). This also leads to an inherent disadvantage, that a long-working distance objective must be used. Consequently, the NA of the objective is low and the area of far-field illumination is large. Considering that the enhanced electromagnetic

field at the tip-sample junction is localized in an area of tens of nanometer, the background induced from the far-field illumination is relatively larger than in the epi-illumination method discussed above. Similar to the lightning rod effect, the existence of a p-polarized component of the illumination is crucial to excite the gap mode and only this component can be greatly enhanced (Aravind and Metiu 1983). Table 1 summarizes the experimental configurations used for tip-enhanced Raman scattering.

Table 1: Setups for tip-enhanced Raman spectroscopy (TERS).

Illumination / detection	Angle (beam-tip axis)	Feedback mechanism	Refs.	
Epi-illumination / transmission	Inverted microscope (NA 1.4)	180°	AFM (contact mode)	(Stöckle, Suh, Deckert and Zenobi 2000, Wang, Smith, Batchelder, Saito, Kirkham, Robinson, Baldwin, Li and Bennett 2003)
		180°	AFM (tapping mode)	(Bulgarevich and Futamata 2004)
		180°	Shear-force tip feedback (tuning fork)	(Hartschuh, Anderson and Novotny 2003, Hartschuh, Sanchez, Xie and Novotny 2003, Stöckle, Suh, Deckert and Zenobi 2000)
		180°	STM	(Pettinger, Picardi, Schuster and Ertl 2003)
	Illumination under total internal reflection (TIR) using an inverted microscope (NA 1.4)	TIR illumination, 180° detection	AFM (contact mode)	(Hayazawa, Inouye, Sekkat and Kawata 2000, 2001, Hayazawa, Tarun, Inouye and Kawata 2002)
Conventional microscope	180°	AFM (contact mode)	(Anderson 2000b)	
Laser beam focused using one single lens	180°	Ag coated silica fiber tip in x-y-z micropositioning stage	(Stokes, Chi and Vo-Dinh 2004)	
Side illumination / reflection	Conventional microscope (NA 0.3 - 0.6)	~ 90°	AFM (contact mode)	(Anderson and Pike 2002)
		65°	AFM (contact mode)	(Mehtani, Lee, Hartschuh, Kisliuk, Foster, Sokolov and Maguire 2005a, 2005b)
		60°	STM	(Pettinger, Picardi, Schuster and Ertl 2003)
		45°	Shear-force tip feedback (tuning fork)	(Atesang and Geer 2005)
		45°	AFM (contact mode)	(Wu, Wang, Wang, Tian and Yu 2005)
	~ 0°	AFM (contact mode)	(Sun and Shen 2001)	
Side illumination / transmission	Conventional microscope (NA 0.35 - 0.55), detection using an inverted microscope (NA 0.6 - 1.4)	80° illumination, 180° detection	AFM (contact mode)	(Hayazawa, Tarun, Inouye and Kawata 2002)
		45° illumination, 180° detection	AFM (tapping mode)	(Nieman, Krampert and Martinez 2001)

2.2. Tip-enhanced Coherent Anti-Stokes Raman Scattering (TE-CARS)

Field enhancement by a sharp tip is also used in non-linear Raman spectroscopy. The most interesting method in this area is coherent anti-Stokes Raman scattering (CARS). It has great potential for bio-sample imaging, because of its low noise and its high penetration depth ability in biological samples. CARS is a four-wave mixing spectroscopic method. It uses three laser beams with two frequencies – twice ω_1 and once ω_2 ($\omega_1 > \omega_2$) – to generate an anti-Stokes field with a frequency of $\omega_{as} = 2\omega_1 - \omega_2$ as shown in Fig. 2. The frequency of the signal is higher than that of the excitation lasers making it a fluorescence free method. Both far-field and near-field CARS have been demonstrated recently (Ichimura, Hayazawa, Hashimoto, Inouye and Kawata 2004a, Zumbusch, Holtom and Xie 1999). For near-field CARS measurements, the group of Kawata employed an inverted microscope for epi-illumination of an Ag-coated AFM tip (Ichimura, Hayazawa, Hashimoto, Inouye and Kawata 2004a, 2004b). For excitation, two Ti:sapphire lasers were used, which generate near-IR radiation with frequencies of ω_1 and ω_2 , respectively. By keeping ω_1 (pump laser) constant and tuning ω_2 (Stokes laser) over a certain range, bands at Raman shifts of $\omega_{Raman} = \omega_1 - \omega_2$ can be investigated.

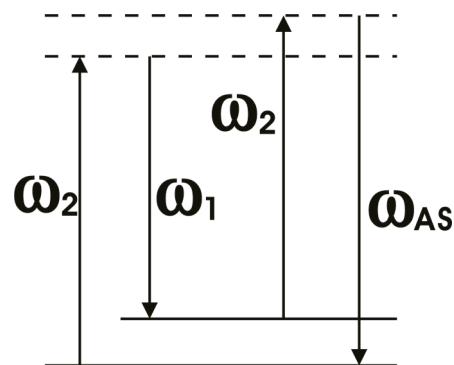


Fig. 2: Illustration of CARS

2.3. Scattering Scanning Near-field Optical Microscopy (s-SNOM)

Near-field IR microscopy has also been developed in various groups during the last ten years. One of most successful schemes is the s-SNOM setup developed in the group of Keilmann (Hillenbrand, Taubner and Keilmann 2002, Knoll and Keilmann 1999). Different from TERS, it is not based on the giant enhancement of EM field at the tip end, but the localized perturbation of the electromagnetic field induced by the tip-sample interaction (Taubner, Hillenbrand and Keilmann 2004). Modeling the tip as a sphere with a radius of a , at a distance d from a substrate, this interaction can be described by an effective polarizability using the dipole approximation:

$$\alpha_{\perp}^{eff} = \frac{\alpha(1 + \beta)}{1 - \frac{\alpha\beta}{16\pi(a + d)^3}}$$

where $\beta = \frac{\epsilon_s - 1}{\epsilon_s + 1}$, $\alpha = 4\pi a^3 \frac{\epsilon_t - 1}{\epsilon_t + 2}$, ϵ_t and ϵ_s denote the dielectric constants of the tip and the sample, respectively. In this case, the scattering response can be described by $\sigma = E_s / E_i = \alpha_{\perp}^{eff}$ where the E_s and E_i denote the intensities of the scattering field and the incident field, respectively. In practice, the value of α_{\perp}^{eff} can be obtained by an interferometric s-SNOM (Taubner, Hillenbrand and Keilmann 2003). Consequently, the value of the optical constants of the sample can be determined with high spatial resolution. This is an elegant and successful approach. It has been proven experimentally with special samples of flat polymer films. On the other hand, this mode of operation is not yet suitable for investigating complex, real-life samples, because it requires a very flat surface. Also, a spherical tip is assumed to derive the polarizability, and in our opinion the methodology still needs further validation.

Narita and Kimura presented a combination of FTIR with SPM, where an Au coated etched glass fiber probe was side-illuminated by the output of a FTIR spectrometer (Narita and Kimura 2001). Detection was performed in reflection mode using a InSb detector whose signal was sent back to the FTIR spectrometer. Since no enhancement could be achieved for white light illumination, the contrast between near-field signal and background was comparatively low. The estimated lateral resolution of $< 2.5 \mu\text{m}$ is also poor compared to s-SNOM experiments with monochromatic excitation but demonstrates sub-wavelength resolution with respect to the mid-infrared wavelength used for illumination. Table 2 summarizes the experimental s-SNOM configurations used by various research groups.

Table 2: Setups for scattering scanning near-field optical microscopy (s-SNOM).

Illumination / detection		Angle (beam-tip axis)	Feedback mechanism	Refs.
Side illumination / reflection	Conventional microscope (NA 0.28 ... 0.55)	60°	AFM (tapping mode)	(Hillenbrand and Keilmann 2000)
		60°	STM	(Barbara, Lopez-Rios and Quémenerais 2005)
		80°	AFM (tapping mode)	(Akhremitchev, Sun, Stebounova and Walker 2002)
	FTIR spectrometer and focusing mirror	(not reported)	Shear-force feedback with optical detection	(Narita and Kimura 2001)

An alternate way to measure optical absorption at the nanometer scale is to combine scanning probe microscopy (SPM) techniques with the photothermal effect, which describes the heating of a sample due to absorption of electromagnetic radiation. Chopped irradiation of the junction region of an STM leads to periodic heating and cooling of tip and sample. Since both are made of different materials, the result is a measurable potential difference. The first demonstration of this technique by the group of Wickramasinghe was applied to optical absorption measurements in the visible spectral range (Weaver, Walpita and Wickramasinghe 1989). A similar Kelvin probe force microscope that is based on detection of photothermal

signals by a modified AFM setup was applied also to this spectral range (Nonnenmacher, Oboyle and Wickramasinghe 1991, Nonnenmacher and Wickramasinghe 1992). Apertureless photothermal near-field measurements in the IR range use a detection concept that is based on photoacoustic spectroscopy. This technique takes advantage of the volume expansion caused by photothermal heating. The resulting acoustic or ultrasonic waves lead to surface deflections, which can be detected by AFM (Anderson 2000a, Tomoda, Shiraishi, Kolosov and Wright 2003) or STM (Hida, Mera and Maeda 2001). These techniques not only add an additional optical contrast to SPM images, they also have great potential for the detection of buried subsurface structures as well as possible depth-resolved measurements.

2.4. Tip fabrication

The tip has direct effect on the degree of TERS enhancement, and consequently, the signal intensity and S/N ratio. Its fabrication procedure is thus of great importance for the performance of TERS as an analytical tool. The type of tip used is closely related to the method to control the tip-sample distance. Three types of SPM techniques are used in TERS, and they are shear-force feedback using a tuning fork, AFM with a cantilever, and the STM (Table 1). Almost all kinds of tips can be used in the tuning fork based shear-force mode (Hartschuh, Sanchez, Xie and Novotny 2003, Stöckle, Suh, Deckert and Zenobi 2000), but it can be tedious to attach the probe properly to the tuning fork to achieve a good feedback. The AFM is the most universal, versatile and robust method for surface analysis, with the advantage of being able to obtain complementary data such as friction force, electric force, magnetic force, or phase images simultaneously with the topography image.

Two types of methods have been used to metallize the AFM tips: the widely used physical deposition (sputter or vapor coating) (Hayazawa, Inouye, Sekkat and Kawata 2000, Stöckle, Suh, Deckert and Zenobi 2000) and chemical deposition (Ag mirror reaction) (Wang, Saito, Batchelder, Kirkham, Robinson and Smith 2005). There are three

disadvantages of the AFM based TERS. First, while vapor-coated AFM tips are easy to prepare, the enhancement factors obtained in this fashion are known to vary a lot. This can be attributed to the fact that the physical deposition process is stochastic and the probability of obtaining a suitable ‘hot’ particle on the tip apex is typically low (Anderson and Pike 2002). Secondly, the metal coating can influence the performance of the cantilever. Heating of the cantilever during fast vapor deposition rates is known to lead to its distortion and makes it unsuitable to use for scanning (Hayazawa, Inouye, Sekkat and Kawata 2002). The adhesion of the metal coating to the silicon tip is also weak and peels off easily after several hours of scanning as shown in Fig. 3 (a) and Fig. 3 (b) (Nieman, Krampert and Martinez 2001). Finally, AFM tips are prohibitively expensive. The use of Ag-mirror coated tips has yet to be reported by other groups presumably due to its longer time and steps of preparation.

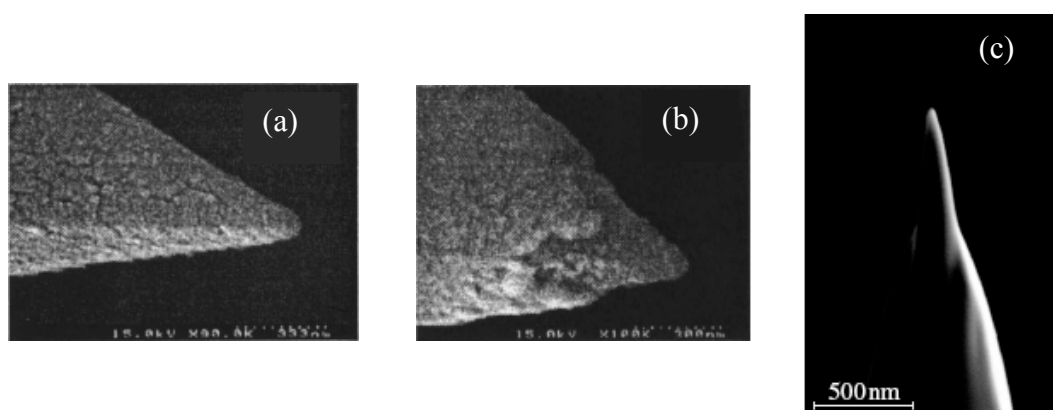


Fig. 3: SEM images of (a) an unused gold vapor-coated AFM tip and (b) the same tip after approximately 10 h of AFM imaging. It is evident that the gold wears away from the tip end with use, affecting the surface enhancement over time. (c) An electrochemically etched tip Ag tip sharpened by focused ion milling. Fig. 3 (a) and Fig. 3 (b) reprinted from (Nieman, Krampert and Martinez 2001), with permission of the American Institute of Physics. Fig. 3 (c) reprinted with permission from (Hartschuh, Sanchez, Xie and Novotny 2003). Copyright (2003) by the American Physical Society.

Compared to the tuning fork scheme and AFM, the fabrication of the STM tip is easier and cheaper. The art of producing sharp metallic tips by electrochemical etching with optional focused ion beam milling (FIB) for tip sharpening have been developed in the past 20 years (Fig. 3 (c)) (Hartschuh, Sanchez, Xie and Novotny 2003, Ren, Picardi and Pettinger

2004). The best Raman enhancement to date has been reported from STM based TERS studies (Pettinger, Ren, Picardi, Schuster and Ertl 2004, Ren, Picardi, Pettinger, Schuster and Ertl 2005). Unfortunately, STM based TERS requires conductive samples, which severely limits its application.

The material of the irradiated part of the tip is of great importance to whether it exhibits strong TERS enhancement with samples. This is related to the ability to create an enhanced electromagnetic field from the localized surface plasmon polariton at the tip apex during radiation by the excitation laser (Demming, Festy and Richards 2005). Ag and Au are the two metals used with visible light excitation. The main advantage of Ag is that the imaginary part of its permittivity is much smaller than that of Au, which leads to a higher field enhancement. While Ag or Ag coated tips have the advantage of being more compatible with a 488-nm laser, its enhancement is known to degrade rapidly due to oxidation (Watanabe, Ishida, Hayazawa, Inouye and Kawata 2004). Au or Au coated tips are used by some groups and are chemically durable for months (Mehtani, Lee, Hartschuh, Kisliuk, Foster, Sokolov and Maguire 2005b). It has been reported that the tips produced by the same etching procedure produce measurable enhancements that vary from negligible to several orders of magnitude (Hartschuh, Sanchez, Xie and Novotny 2003, Pettinger, Ren, Picardi, Schuster and Ertl 2004). There has been contrasting information on the methods to make a Raman enhancement tip. For instance, both Au and Ag etched tips have been used with a He-Ne laser (633 nm) with similar Raman enhancement levels of 10^3 - 10^4 (Anderson, Hartschuh, Cronin and Novotny 2005, Hartschuh, Sanchez, Xie and Novotny 2003). We believe that the ability to reproducibly fabricate a tip that exhibits consistently good TERS enhancement with a particular excitation wavelength is necessary for the widespread application of TERS for nanoscale chemical analysis. Theoretical investigations that provide guidelines for fabricating tips with strong Raman enhancement will be very useful. An alternative is to employ a

tunable laser to tune into the correct surface plasmon resonance of the TERS-active metal particle.

3. Enhancement Factors and Lateral Resolution

The feasibility of a TERS application depends mainly on the extent of field enhancement that can be obtained. In several publications on TERS, enhancement factors for a certain combination of setup and sample are presented. Based on these values, comparisons between TERS and SERS measurements, experimental and theoretical data as well as comparisons between different TERS studies are possible. In the literature, several different ways of calculating TERS enhancement factors have been presented, which makes it difficult to directly compare the results. In this section we therefore discuss the various definitions of the TERS enhancement factor which are in use by different groups, and give an overview on published values and the basis for their calculation. This should help the readers to assess more critically these enhancement factors and to choose the appropriate way for estimation of enhancement factors in further TERS studies. Finally, a short comparison of the lateral resolution that has been achieved in apertureless near-field optical microscopy experiments is given.

3.1. TERS Contrasts and Enhancement Factors

The calculation of TERS enhancement factors consists of two parts. First, the contrast between the near-field and far-field signals is derived from measured values. Second, based on this contrast, the enhancement factor is calculated, taking into account that the sources of far-field and near-field signal are of different size.

The contrast is defined as the ratio between near-field and far-field signal. It has been determined by measuring Raman signals with the tip in contact with the sample and with the tip retracted, respectively (Bulgarevich and Futamata 2004, Nieman, Krampert and Martinez

2001, Pettinger, Ren, Picardi, Schuster and Ertl 2004, Stokes, Chi and Vo-Dinh 2004, Stöckle, Suh, Deckert and Zenobi 2000).

Definition (a):
$$\text{Contrast} = \frac{I_{\text{with tip}}}{I_{\text{without tip}}}$$

A more precise definition takes into account that the far-field signal is present as a background also when the tip is in contact with the sample. Here, the near-field signal is defined as the difference between the signal intensities obtained with and without the tip (Hartschuh, Anderson and Novotny 2003, Hayazawa, Inouye, Sekkat and Kawata 2000, Mehtani, Lee, Hartschuh, Kisliuk, Foster, Sokolov and Maguire 2005b, Patanè, Gucciardi, Labardi and Allegrini 2004, Sun and Shen 2001, Wang, Smith, Batchelder, Saito, Kirkham, Robinson, Baldwin, Li and Bennett 2003). This leads to a contrast value of:

Definition (b):
$$\text{Contrast} = \frac{I_{\text{near field}}}{I_{\text{far field}}} = \frac{I_{\text{with tip}} - I_{\text{without tip}}}{I_{\text{without tip}}} = \frac{I_{\text{with tip}}}{I_{\text{without tip}}} - 1$$

In our opinion, definition (a) is of higher practical relevance because it is an indicator for the quality of TERS near-field images that can be achieved in a certain combination of setup and sample. On the other hand, definition (b) allows a more precise estimation of the field enhancement and is therefore more useful in comparisons between experimentally determined and theoretically calculated data. Since the difference between both definitions is one, the method of calculation affects only small contrast values significantly. In the case of small near-field signals and/or high far-field background contributions, definition (b) can lead to contrasts that are < 1 . An increase of this value can be achieved by increasing the near-field enhancement by means of an appropriate tip, by minimizing the far-field background signal, or by the best possible compromise between both strategies.

As mentioned above, the enhancement factor also takes into account that the sources of the near-field and far-field signals are different. These signals have to be normalized to the corresponding illuminated areas (Definition (c)) or volumes (Definition (d)) (Anderson 2000b, Hayazawa, Inouye, Sekkat and Kawata 2000, Nieman, Krampert and Martinez 2001, Pettinger, Ren, Picardi, Schuster and Ertl 2004, Stokes, Chi and Vo-Dinh 2004, Stöckle, Suh, Deckert and Zenobi 2000, Wang, Smith, Batchelder, Saito, Kirkham, Robinson, Baldwin, Li and Bennett 2003) (Bulgarevich and Futamata 2004, Hartschuh, Sanchez, Xie and Novotny 2003, Mehtani, Lee, Hartschuh, Kisiuk, Foster, Sokolov and Maguire 2005b, Patanè, Gucciardi, Labardi and Allegrini 2004, Sun and Shen 2001).

$$\text{Definition (c):} \quad \text{Enhancement factor} = \text{Contrast} \times \frac{A_{\text{focus}}}{A_{\text{tip}}} = \text{Contrast} \times \frac{d_{\text{focus}}^2}{d_{\text{tip}}^2}$$

$$\text{Definition (d):} \quad \text{Enhancement factor} = \text{Contrast} \times \frac{V_{\text{focus}}}{V_{\text{near field}}} = \text{Contrast} \times \frac{d_{\text{focus}}^2}{d_{\text{tip}}^2} \times \frac{h_{\text{focus}}}{h_{\text{near field}}}$$

Here, d_{focus} and h_{focus} are diameter and height of the laser focus, d_{tip} is generally taken as two times the radius of curvature of the tip, and $h_{\text{near field}}$ is the estimated depth of the near field. In the case of the enhancement factor, the choice of the definition and the estimated values of the source dimensions sizes have a strong influence on the result. In the case of thin or opaque samples, calculations based on the focal height can lead to an overestimation of the far-field volume and thus to an overestimation of the enhancement factor. Therefore, the group of Sokolov proposed to multiply the focal area with the smallest of the following three quantities: the sample thickness, the light penetration depth, and the height of the focus (Mehtani, Lee, Hartschuh, Kisiuk, Foster, Sokolov and Maguire 2005b).

Estimation of the near-field source size is much more problematic, because this value cannot be measured directly. In most cases, the corresponding area is calculated using the relatively well known curvature radius of the tip, even though theoretical studies and some

experimental results suggest that the source of the near-field enhancement can be smaller than the area under the tip (Demming, Festy and Richards 2005, Hartschuh, Anderson and Novotny 2003, Mills 2002, Ren, Picardi, Pettinger, Schuster and Ertl 2005). If definition (d) is used, the height of the near field has to be estimated (Bulgarevich and Futamata 2004, Sun and Shen 2001). From evaluation of the TERS enhancement factor as a function of the thickness of CdS films, $h_{\text{near field}} = 20 \pm 5$ nm was obtained for an Ag-coated tip with radius 25 nm (Mehtani, Lee, Hartschuh, Kisliuk, Foster, Sokolov and Maguire 2005b). A plot of signal intensity versus distance between a tip (10-15 nm radius) and a SWNT sample resulted in a $h_{\text{near field}} = 11$ nm (Hartschuh, Sanchez, Xie and Novotny 2003).

Since every combination of the contrast definitions (a) and (b) with the definitions of the enhancement factor (c) and (d) is possible, there are four ways to calculate the enhancement factor, which are in use by different groups. For convenience, we use the following abbreviations for these combinations: (a)+(c), (a)+(d), (b)+(c), and (b)+(d). An example should demonstrate how the definitions of the enhancement factor influence the calculation result. Sun and Shen (2001) published TERS measurements of silicon surfaces. The bulk sample was relatively thick compared to the thin films investigated in other studies. This results in an increased far field background and thus in a lower contrast value. As mentioned above, small contrast values depend significantly on the definition that was used for their calculation. With the tip in contact, the intensity of the Raman signal was 1 a.u., whereas with the tip retracted the signal decreased to 0.65 a.u. For calculation of far-field and near-field volume, the authors estimated the following values: $d_{\text{focus}} = 3 \mu\text{m}$, $h_{\text{focus}} = 500$ nm, $d_{\text{tip}} = 100$ nm, and $h_{\text{near field}} = 20$ nm.

The height of the focus equals approximately to the light penetration depth of 515 nm radiation in silicon (Mehtani, Lee, Hartschuh, Kisliuk, Foster, Sokolov and Maguire 2005b), whereas the sample thickness was much higher. Thus, these values are in agreement with the method for estimation of the far-field volume mentioned above, which was proposed by the

group of Sokolov (Mehtani, Lee, Hartschuh, Kisliuk, Foster, Sokolov and Maguire 2005b). When the same values are used, the four definitions of the enhancement factor lead to significantly different results:

Definition (b)+(c): Contrast = 0.54; Enhancement factor = 4.9×10^2

Definition (a)+(c): Contrast = 1.54; Enhancement factor = 1.4×10^3

Definition (b)+(d): Contrast = 0.54; Enhancement factor = 1.2×10^4 (reported by Sun and Shen)

Definition (a)+(d): Contrast = 1.54; Enhancement factor = 3.4×10^4

In both cases, contrast definition (a) leads to a value that is $\sim 3 \times$ the result of definition (b). The enhancement factor is increased further, when definition (d) is used instead of (c) because of the additional factor $h_{\text{focus}} / h_{\text{near field}}$ that is $500 \text{ nm} / 20 \text{ nm} = 25$ in this case. These two effects lead to a ratio of ~ 70 between the highest and lowest enhancement factor in this example, i.e. between (a)+(d) and (b)+(c). It should be pointed out that uncertainties of the estimated diameters and heights affect the result additionally. Since the enhancement factor depends on the square of the diameter, a slightly different value can change the result considerably. We conclude that estimated areas and volumes as well as the way of calculation could change the enhancement factor by approximately two orders of magnitude. Since most of the TERS enhancement factors published to date range over approximately two orders of magnitude from 10^2 to 10^4 , a comparison of different studies is only possible if the method and estimated values that were used for the calculation are known. Therefore, comparison of contrasts and enhancement factors in Table 3 contains additional information on the calculation method and parameters such as d_{focus} , h_{focus} , d_{tip} , and $h_{\text{near field}}$.

Pettinger *et al.* proposed an alternate way to calculate the TERS enhancement factor (Pettinger, Ren, Picardi, Schuster and Ertl 2004, 2005):

Definition (e): Enhancement factor = g^4

Here, the enhancement factor is derived from the electric field enhancement g , which is estimated by evaluating the temporal bleaching behavior of the sample. The main advantage of this method is its independence from estimated sizes of the involved signal sources. The resulting enhancement factor can also be used to calculate the near-field volume.

3.2. Comparison of TERS Contrasts and Enhancement Factors

TERS enhancement factors reported in literature range from $16 - \sim 6 \times 10^6$ (Table 3). Whereas most of them lie between 10^2 and 10^4 , recent studies have reported values in the 10^5 to 10^6 range. The highest enhancement factors have been achieved by the group of Pettinger using an Au STM tip with 60° side illumination in reflection mode ($\lambda = 633$ nm) (Pettinger, Ren, Picardi, Schuster and Ertl 2004, 2005). Here both definitions (a)+(c) and (e) resulted in enhancement factors ranging from $4 \times 10^5 - 6 \times 10^6$. These enhancement factors are connected to contrasts that are more than two orders of magnitude higher than the corresponding values obtained in other studies. This huge effect can be attributed in part to highly intense gap mode plasmons as well as resonance Raman scattering, and carefully selected polarization and incidence angles of the exciting laser beam.

The group of Sokolov could raise the contrast that was achieved in TERS measurements of silicon surfaces from 0.3 up to 12 by optimizing the polarization of the excitation beam (Mehtani, Lee, Hartschuh, Kisliuk, Foster, Sokolov and Maguire 2005a, 2005b). In this case, polarization optics have been used for both, with improvement of the near-field enhancement and suppression of the far-field background signal. The authors selected a highly polarized Raman band of silicon for their experiments. The corresponding far-field signal can be suppressed when the measurements are performed in a depolarized geometry. On the other hand, a metallized TERS probe in contact with the sample enhances

and depolarizes the Raman emission, which is therefore transmitted by the analyzer. The best compromise between strong Raman enhancement with polarization parallel to the tip axis and good suppression of the far-field background was found at polarization angles between 50 and 70° with respect to the tip axis. The optimum angle of the analyzer depended on sample material and orientation and was optimized additionally. In this way, the enhancement factor according to definition (b)+(d) could be increased from 1.2×10^4 to 5×10^5 .

It must be mentioned here that the sample quality will affect the Raman enhancement as well. For instance, for dye molecules spin-coated on glass slides, it is difficult to obtain a completely flat layer and there is a tendency for small crystals to form. If the tip is placed on an isolated crystal and TERS is measured, it is likely that the TERS enhancement be much higher. The same caution should be applied for systems such as SWNTs where it is impossible to form a uniform layer.

Table 3: Comparison of TERS enhancement factors obtained with diverse tips, samples, and excitation wavelengths. (a)-(e) refer to different definitions of contrast and enhancement factor (see text). CM: contact mode, TM: tapping mode, TIR: total internal reflection, d: diameter, w: width, h: height.

Tip	Sample	Excitation wavelength	Estimated source size	Contrast	Enhancement factor	Ref.
AFM CM tip coated with Ag	Brilliant cresyl blue (BCB)	488 nm	$d_{\text{focus}} = 300 \text{ nm}$ $d_{\text{tip}} = 50 \text{ nm}$	30 ^(a)	2×10^3 ^(c)	(Stöckle, Suh, Deckert and Zenobi 2000)
Au tip (shear force)	Fullerenes	488 nm	$d_{\text{focus}} = 300 \text{ nm}$ $d_{\text{tip}} = 20 \text{ nm}$	40 ^(a)	4×10^4 ^(c)	(Stöckle, Suh, Deckert and Zenobi 2000)
AFM CM tip coated with Ag	Sulfur	785 nm	(not reported)	(not reported)	1×10^4 ^(c)	(Anderson 2000b)
AFM CM tip coated with Ag (TIR illum.)	Rhodamine-6G on Ag	488 nm	$d_{\text{focus}} = 400 \text{ nm}$ $d_{\text{tip}} = 40 \text{ nm}$	(not reported)	40 ^{(b)+(c)}	(Hayazawa, Inouye, Sekkat and Kawata 2000)
AFM CM tip coated with Au	Polydiacetylene <i>para</i> -toluene sulfonate (PDA-PTS)	488 nm	$d_{\text{focus}} = 2500 \text{ nm}$ $d_{\text{tip}} = 40 \text{ nm}$	3.4 ^(a)	2×10^4 ^(c)	(Nieman, Krampert and Martinez 2001)
AFM CM tungsten tip	Silicon	488 nm	$d_{\text{focus}} = 3000 \text{ nm}$ $h_{\text{focus}} = 500 \text{ nm}$ $d_{\text{tip}} = 100 \text{ nm}$ $h_{\text{near field}} = 20 \text{ nm}$	0.54 ^(b)	1.2×10^4 ^(d)	(Sun and Shen 2001)
AFM CM tip coated with Ag (TIR illum.)	Rhodamine-6G on Ag	532 nm	$d_{\text{focus}} = 400 \text{ nm}$ $d_{\text{tip}} = 40 \text{ nm}$	1 ^(b)	1×10^2 ^(c)	(Hayazawa, Inouye, Sekkat and Kawata 2002)
AFM CM tip coated with Ag (side illum.)	Rhodamine-6G on Ag	532 nm	$d_{\text{focus}} = 1800 \text{ nm}$ $d_{\text{tip}} = 40 \text{ nm}$	2 ^(b)	4×10^3 ^(c)	(Hayazawa, Tarun, Inouye and Kawata 2002)
AFM CM tip coated with Ag (TIR illum.)	Adenine	532 nm	$d_{\text{focus}} = 400 \text{ nm}$ $d_{\text{tip}} = 30 \text{ nm}$	(not reported)	2.7×10^3 ^(c)	(Hayazawa, Yano, Watanabe, Inouye and Kawata 2003)
AFM CM tip coated with Au	Fullerenes	515 nm	$d_{\text{focus}} = 1000 \text{ nm}$ $d_{\text{tip}} = 100 \text{ nm}$	2 ^(b)	2×10^2 ^(c)	(Wang, Smith, Batchelder, Saito, Kirkham, Robinson, Baldwin, Li and Bennett 2003)
Au tip (shear force)	Single-walled carbon nanotubes (SWNT)	633 nm	$d_{\text{focus}} = 330 \text{ nm}$ $w_{\text{SWNT}} = 20 \text{ nm}$ $h_{\text{SWNT}} = 10 \text{ nm}$ $d_{\text{near field}} = 26 \text{ nm}$ $w_{\text{SWNT}} = 20 \text{ nm}$ $h_{\text{SWNT}} = 10 \text{ nm}$	1.3 ^(b)	16 ^(d)	(Hartschuh, Anderson and Novotny 2003)

Ag tip (shear force)	Single-walled carbon nanotubes (SWNT)	633 nm	(not reported)	(not reported)	1×10^3 ^(d)	(Hartschuh, Sanchez, Xie and Novotny 2003)
AFM TM tip coated with Au	Diamond microparticles	532 nm	$d_{\text{focus}} = 240 \text{ nm}$ $h_{\text{focus}} = 520 \text{ nm}$ $d_{\text{tip}} = 100 \text{ nm}$ $h_{\text{near field}} = 20 \text{ nm}$	5 ^(a)	7.5×10^2 ^(d)	(Bulgarevich and Futamata 2004)
Ag coated silica fiber in micropos. Stage	Brilliant Cresyl Blue (BCB)	633 nm	$d_{\text{focus}} = 50 \mu\text{m} \dots 100 \mu\text{m}$ $d_{\text{tip}} = 100 \text{ nm}$	8 ^(a)	$2 \times 10^6 \dots$ 8×10^6 ^(c)	(Stokes, Chi and Vo-Dinh 2004)
Au STM tip	Chemisorbed CN ⁻ on Au	633 nm	$d_{\text{focus}} = 2000 \text{ nm}$ $d_{\text{tip}} = 80 \text{ nm}$	800 ^(a)	4×10^5 ^(c)	(Pettinger, Ren, Picardi, Schuster and Ertl 2004)
Au STM tip	Malachite green isothiocyanate (MGITC) on Au	633 nm	$d_{\text{focus}} = 2000 \text{ nm}$ $d_{\text{near field}} = 70 \dots 180 \text{ nm}$	4000 ... 14000 (avg. 8000) ^(a)	$1 \times 10^6 \dots$ 7×10^6 ^(e)	(Pettinger, Ren, Picardi, Schuster and Ertl 2004)
Au STM tip	Malachite green isothiocyanate (MGITC) on Au	633 nm	$d_{\text{near field}} = 50 \text{ nm}$	(not reported)	6.3×10^6 ^(e)	(Pettinger, Ren, Picardi, Schuster and Ertl 2005)
AFM CM tip coated with Au	Silicon	515 nm	$d_{\text{focus}} = 1600 \text{ nm}$ $h_{\text{penetration depth}} = 500 \text{ nm}$ $d_{\text{tip}} = 40 \text{ nm}$ $h_{\text{near field}} = 20 \text{ nm}$	0.3 ^(b)	1.2×10^4 ^(d)	(Mehtani, Lee, Hartschuh, Kisluk, Foster, Sokolov and Maguire 2005b)
AFM CM tip coated with Au	CdS film on aluminum	515 nm	$d_{\text{focus}} = 1600 \text{ nm}$ $h_{\text{sample thickness}} = 10 \text{ nm}$ $d_{\text{tip}} = 40 \text{ nm}$ $h_{\text{near field}} = 20 \text{ nm}$	6 ^(b)	5×10^3 ^(d)	(Mehtani, Lee, Hartschuh, Kisluk, Foster, Sokolov and Maguire 2005b)
AFM CM tip coated with Au (optimized polarization geometry)	Silicon	515 nm	$d_{\text{focus}} = 1600 \text{ nm}$ $h_{\text{penetration depth}} = 500 \text{ nm}$ $d_{\text{tip}} = 40 \text{ nm}$ $h_{\text{near field}} = 20 \text{ nm}$	12 ^(b)	5×10^5 ^(d)	(Mehtani, Lee, Hartschuh, Kisluk, Foster, Sokolov and Maguire 2005a)

Surely, different studies with similar illumination schemes can be better compared based on TERS contrasts. The contrast is derived directly from measured signal intensities and is therefore independent from estimated parameters. Only the definition used, (a) or (b) has to be specified. Beside the better comparability, contrast values are of much higher practical relevance than enhancement factors (Mehtani, Lee, Hartschuh, Kisliuk, Foster, Sokolov and Maguire 2005b). The feasibility of TERS imaging in a given combination of setup and sample depends mostly on the contrast level that can be achieved. Similar to the signal-to-noise ratio, the ratio between near-field signal and far-field background has to be sufficiently high to obtain high-contrast and high-resolution TERS images. The importance of the enhancement factor lies more in its comparability to theoretical calculations of field and TERS enhancement. For example, Sun and Shen as well as Mehtani *et al.* published TERS investigations of bulk silicon samples and achieved a comparatively high enhancement factor of 1.2×10^4 (Mehtani, Lee, Hartschuh, Kisliuk, Foster, Sokolov and Maguire 2005b, Sun and Shen 2001). On the contrary, the corresponding contrast values obtained, 0.54 and 0.3 using definition (b), reveal that TERS near-field imaging is hampered by a strong far-field background contribution.

When converted to definition (b), most published TERS contrast values so far are in the range from 0.3 to 2.4 (see Table 3). The groups of Futamata and Vo-Dinh obtained significantly higher values (Bulgarevich and Futamata 2004, Stokes, Chi and Vo-Dinh 2004). The investigation of diamond microparticles and brilliant cresyl blue (BCB) resulted in contrasts of 4 and 7, respectively, when the published values are converted to definition (b). The huge difference in the corresponding enhancement factors of 7.5×10^2 in the first case and more than 10^6 in the latter can be explained by different far-field volumes that were illuminated. Since the group of Vo-Dinh used a single lens instead of a microscope objective for focusing of the laser beam, the far-field background was generated on a significantly larger area than in the experiments of Bulgarevich and Futamata.

Until now, the highest TERS contrast values have been achieved by the groups of Zenobi and Pettinger. In the first experimental demonstration of the TERS effect, Stöckle *et al.* obtained contrasts of 30 in the case of BCB and 40 in the case of C₆₀ (Stöckle, Suh, Deckert and Zenobi 2000). For the measurements, Ag coated AFM tips in contact mode and Au tips in shear-force feedback were used. The tips were illuminated in transmission mode by means of an inverted microscope ($\lambda = 488$ nm). Pettinger *et al.* performed TERS measurements of chemisorbed CN⁻ on Au surfaces and obtained a contrast value of 800, which could be even improved by approximately one order of magnitude in the case of a malachite green isothiocyanate (MGITC) film on Au leading to contrast values that ranged from 4,000 up to 14,000 (Pettinger, Ren, Picardi, Schuster and Ertl 2004). As already mentioned, this group applied an Au STM tip in side illumination geometry ($\lambda = 633$ nm).

TERS measurements on silicon surfaces have to be discussed separately, because they are the only bulk samples in TERS experiments described up to now. In most other experiments, thin layers with a thickness of few tens of nanometers were analyzed. If a bulk sample is irradiated with light having a considerable penetration depth in this material, a far-field background signal is generated that is much higher than in the case of thin film samples and the contrast is decreased considerably. From this point of view, the contrast of 12 that could be reached by Mehtani *et al.* is remarkable (Mehtani, Lee, Hartschuh, Kisliuk, Foster, Sokolov and Maguire 2005a). As mentioned above, this value could be improved from 0.3 up to 12 by optimizing the polarization angles of excitation beam and analyzer. The setup was based on an Au coated AFM tip in contact mode and 65° side illumination in reflection mode ($\lambda = 515$ nm).

3.3. Lateral Resolution in Apertureless Near-field Microscopy

A good estimate for the lateral resolution that can be achieved in TERS imaging is the tip apex diameter which can be determined by SEM. The tip diameters listed in Table 3 range from 20 to 100 nm, allowing imaging with sub-wavelength resolution in every case. In several cases, etched metal tips that can be used in shear-force feedback or in STM setups enable higher lateral resolutions than metal coated AFM probes because of the larger radii of curvature of the latter. Some experimental results suggest that the lateral resolution of a TERS image can be even better than the resolution of the corresponding topography image and thus have a smaller value than the tip diameter (Hartschuh, Anderson and Novotny 2003, Saito, Hayazawa, Kataura, Murakami, Tsukagoshi, Inouye and Kawata 2005). Up to now, the highest spatial resolutions achieved in TERS experiments are in the range of 10-20 nm (Anderson, Hartschuh, Cronin and Novotny 2005, Hartschuh, Sanchez, Xie and Novotny 2003, Saito, Hayazawa, Kataura, Murakami, Tsukagoshi, Inouye and Kawata 2005). Some s-SNOM studies have shown a significantly increased lateral resolution. Whereas measurements in the IR range ($\lambda = 10.6 \mu\text{m}$) could be performed with a resolution of $\sim 17 \text{ nm}$ (i.e. $\lambda/600$) (Lahrech, Bachelot, Gleyzes and Boccara 1996), similar measurements in the visible spectral range revealed the potential for a further improvement of this value. With excitation at $\lambda = 633 \text{ nm}$ s-SNOM imaging provided material-specific contrast with a lateral resolution of $\sim 10 \text{ nm}$ (Hillenbrand and Keilmann 2002). Other studies claimed a lateral resolution as low as 1 nm (Zenhausern, Martin and Wickramasinghe 1995).

4. Chemical Applications

4.1. Dyes

In many cases, the starting point in tip-enhanced vibrational spectroscopy experiments is the study of thin films of dye molecules such as brilliant cresyl blue, rhodamine dyes, or Malachite green isothiocyanate (Hayazawa, Inouye, Sekkat and Kawata 2000, 2002, Hayazawa, Tarun, Inouye and Kawata 2002, Pettinger, Ren, Picardi, Schuster and Ertl 2004, 2005, Stokes, Chi and Vo-Dinh 2004, Stöckle, Suh, Deckert and Zenobi 2000). While there are no particularly interesting aspects of investigating spin-cast films of dyes with spatially resolving techniques such as TERS, dyes have two features that are advantageous from a practical point of view: (i) in many cases, the Raman enhancement can be estimated by comparing against the intensity of unenhanced Raman bands or with the fluorescence background; and (ii) often, one can profit from an additional resonance enhancement if the incident laser wavelength overlaps with the absorption band of the dye. In that sense, dyes are quite different from other organic compounds and may not be representative of the signal levels and enhancement factors one can expect for molecules lacking chromophores. A classic example is shown in Figure 4, the spectrum published by Stöckle *et al.* which is one of the first TERS experiments that has appeared in the literature (Stöckle, Suh, Deckert and Zenobi 2000).

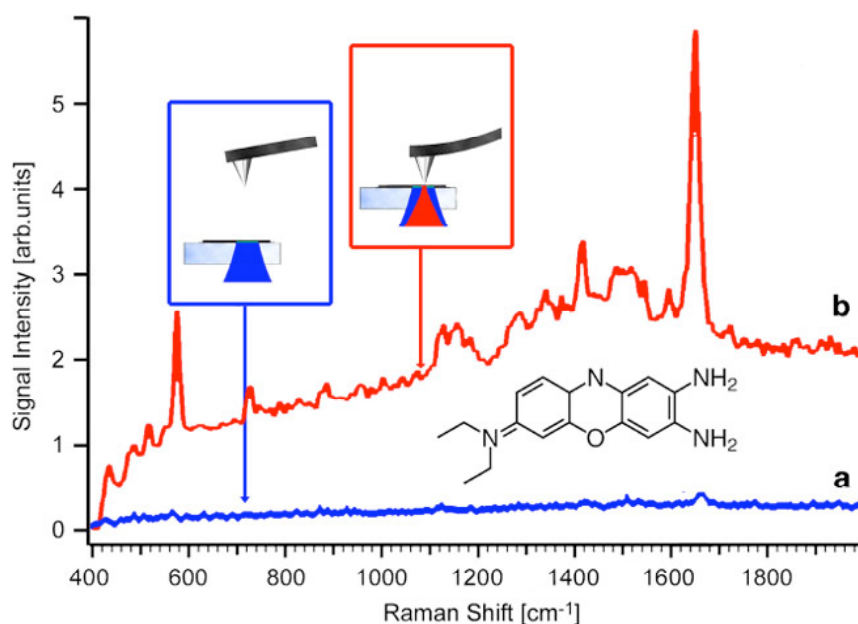


Fig. 4: Tip-enhanced Raman spectra of brilliant cresyl blue dispersed on glass, measured with an AFM tip vapor-coated with silver. The two Raman spectra are measured with the tip retracted from the sample (a) and with the tip in contact with the sample (b). The acquisition time was 60 s per spectrum. The enhancement factor is estimated to be $\sim 2,000\times$, based on a 300 nm diam. illumination beam and a tip apex diameter of 50 nm. This particular example corresponds to the first entry (row) in Table 3 above. Adapted from (Stöckle, Suh, Deckert and Zenobi 2000).

4.2. Catalysis

Catalytic surfaces are attractive for investigation by TERS for a number of reasons. First, it is expected that chemical turnover takes place very locally, at “hot spots” of the catalyst surfaces. Second, catalytic reactions typically happen at elevated pressures and temperatures, i.e., conditions that are very far from those present in ultra high vacuum surface science. Much effort has been invested in overcoming this “pressure gap” for understanding catalysis at relevant conditions (Cremer, Su, Somorjai and Shen 1998, Somorjai and Rupprechter 1999); TERS in principle has the capability to study catalysis at high pressures and temperatures. Many industrially relevant catalysts are supported metal catalysts meaning that finely dispersed metal grains on an inert support such as silica, alumina, etc. are the active sites. These metal grains can lead to additional Raman enhancement, although this

might complicate the data interpretation because transformations occurring on the support may not be observed with the same sensitivity.

Fokas and Deckert (2002) presented a study where aperture SNOM in combination with SERS was used to study Pd-Ag catalyzed hydrogenation of benzene to cyclohexane on a nanofabricated supported Pd-Ag/SiO₂ substrate (see Fig. 5), with a resolution of ~ 100 nm. The idea of studying model catalysts, albeit single crystal surfaces in this case, has also been mentioned in the context of TERS (Ren, Picardi, Pettinger, Schuster and Ertl 2005). The problem that was to be overcome in this case is that single crystal metal surfaces show no or negligible SERS activity due to the absence of surface roughness, preventing SERS studies of adsorbates on single crystal model catalyst surfaces. An external STM tip was therefore used to locally enhance the Raman scattered light from benzenethiol layers on Pt(110) and Au(110). A 20-fold difference in the Raman intensities on Au and Pt was found, which can be ascribed to the different optical properties of these two metals. A control experiment was performed to verify the results and to exclude the presence of measurement artifacts.

We predict that the study of catalytically active surfaces – or at least model catalysts – with TERS will be a very fruitful area of application (Tian, Ren and Wu 2002). If systems can be found whose corrugation is sufficiently small, and once the question how the heterogeneous nature of catalyst surfaces influences the local SERS enhancement has been properly addressed, the spatial resolution, chemical information content, and the possibility to operate at relevant pressures and temperatures of TERS has enormous potential to address important questions in catalysis.

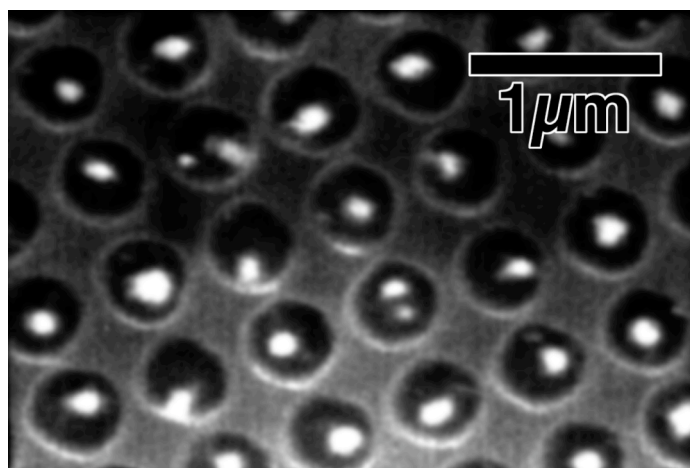


Fig. 5: SEM image of a nanofabricated model catalyst. The support consists of SiO₂ on Si which was etched by a photolithographic / interference technique. This step was followed by metallization with Pd, before removal of the remaining photoresist. By annealing, the metal that is left in the small indentations finally contracts to a small metal structure at the bottom of each indentation.

4.3. Microfluidics and Chromatography

Shear-driven chromatography (SDC) performed in miniaturized channels has been demonstrated to be a potential tool for rapid separation of small quantities of materials. Recently, mixtures of angiotensin peptides or coumarin dyes have been separated using such microfluidic devices at short distances of ≤ 2 mm (Clicq, Vankrunkelsven, Ranson, De Tandt, Barn and Desmet 2004, Vankrunkelsven, Clicq, Cabooter, De Malsche, Gardeniers and Desmet 2006).

Detection of samples is a limitation of SDC. To overcome this problem, a TERS setup has been used by Anderson for the manipulation and analysis of low-volatility fluids flowing in open microchannels with groove widths and depths of 950 and 125 nm, respectively (Anderson 2005). Contact AFM probes have been shown to function like shear plates to move liquids placed in these open grooves. Chemical identification of the liquids can be made by parking an Au coated SERS-active AFM tip in the filled groove. In the experiment reported, ricinoleic acid placed in the channel migrated up onto the tip and cantilever by capillary action. The tip was then retracted and SERS spectrum measured at the cantilever

shows the presence of the acid. If only very small amount of material can be removed, the SERS spectrum could be acquired at the tip end.

While this experiment would not be generally classified as TERS imaging, it does show the versatility of the instrument for different chemical applications. Issues on the practicality of this setup for chemical analysis do remain. For instance, in order to perform rapid identification of different types of liquids without cross-contamination, it is necessary to develop an *in situ* method to regenerate the surface of the SERS-active tip after each measurement. Otherwise, the tip has to be changed or cleaned by rinsing in solvents. Since the separation distance in SDC experiments would be at least an order of magnitude larger than the scan range of commercial AFMs, modification of the setups would be essential for real applications.

5. Biological Applications

5.1. Biopolymers

Reports in the field of apertureless near-field vibrational spectroscopy for imaging of biopolymers up to now have focused on DNA and the corresponding nucleobases. Near-field Raman spectra of nanocrystals of adenine have been determined by TERS measurements (Hayazawa, Yano, Watanabe, Inouye and Kawata 2003, Watanabe, Ishida, Hayazawa, Inouye and Kawata 2004). In this case, an inverted microscope was employed for epi-illumination ($\lambda = 532$ nm) of an Ag-coated AFM tip. Eight Raman bands which could be observed in the TERS spectra were assigned to certain vibrations of the adenine molecule. The most intense Raman signals are the in-plane ring breathing mode of the molecule (at 739 cm^{-1}) and in-plane combination vibrations of C-H, N-H, C-N, and O-N bonds (at $1,328\text{ cm}^{-1}$), respectively. The TERS shifts differed from known Raman and SERS spectra. These differences could be explained by charge-transfer interactions between adenine and the metallized tip, which were

in good agreement with corresponding density functional theory (DFT) calculations. A detailed discussion of such tip-sample interactions and their effect on TERS spectra can be found in Chapter 5 of this volume. The lateral resolution of the system was estimated to be 30 nm by conducting a one-dimensional scan over an adenine crystal. Taking into account the diameter of the illuminated area ($d_{\text{focus}} = 400 \text{ nm}$), calculation of the enhancement factor for the ring-breathing mode at 739 cm^{-1} resulted in a value of 2.7×10^3 (see Table 3).

The feasibility of tip-enhanced CARS (TE-CARS) measurements of adenine was first demonstrated using immobilized nanoparticles for field-enhancement (Ichimura, Hayazawa, Hashimoto, Inouye and Kawata 2003). Gold particles with a diameter of 60 nm were dispersed and fixed on a coverslip. Subsequently, this substrate was coated with adenine. CARS spectra were collected at isolated particles using a multi-focus CARS microscope (Kobayashi, Fujita, Kaneko, Takamatsu, Nakamura and Kawata 2002), where the frequency of the Stokes laser was tuned from $\omega_2 = 11,431.7 \text{ cm}^{-1}$ ($\lambda_2 = 874.8 \text{ nm}$) to $\omega_2 = 11,381.0 \text{ cm}^{-1}$ ($\lambda_2 = 878.7 \text{ nm}$) and the pump laser frequency was kept constant at $\omega_1 = 12,731.7 \text{ cm}^{-1}$ ($\lambda_1 = 785.4 \text{ nm}$). In this way, Raman shifts $\omega_{\text{Raman}} = \omega_1 - \omega_2$ in the range of 1,300 to 1,350 cm^{-1} could be analyzed. This spectral range contains an intense Raman band at 1,328 cm^{-1} . The particle-enhanced CARS spectra were in good agreement with conventional Raman spectra and revealed enhancement factors of up to 2,000. Two attached particles showed a significantly higher enhancement of $\sim 6,000$.

In a further step, this principle was transferred to a scanning metallized tip (Hayazawa, Ichimura, Hashimoto, Inouye and Kawata 2004). Both, sample and tip were illuminated in transmission mode, using a 1.4 NA objective of an inverted microscope. This TE-CARS setup was applied to the imaging of DNA (Ichimura, Hayazawa, Hashimoto, Inouye and Kawata 2004b). Nanoclusters consisting of poly(dA-dT) were cast and dried on a coverslip. The dimension of the nanoclusters was $\sim 100 \text{ nm}$ in diameter and $\sim 20 \text{ nm}$ in height. TERS spectra of such DNA samples revealed several peaks in the spectral range of 1,200 to

1,500 cm^{-1} . The most intense band at 1,337 cm^{-1} could be assigned to the ring-breathing mode of the purin ring of adenine. TE-CARS imaging of the DNA sample was performed at this on-resonant frequency and at the off-resonant frequency 1,278 cm^{-1} . In the on-resonant TE-CARS image, the DNA nanoclusters could be clearly distinguished from the uncoated part of the coverslip. Here, the TE-CARS image was in good agreement with the simultaneously obtained AFM topography image. However, in the off-resonant scan the TE-CARS signal mostly vanished. Weak residual signals were due to off-resonant contributions from thymine and the DNA backbone. Additional possibilities for nonspecific background signals are related to the metallized probe tip (Ichimura, Hayazawa, Hashimoto, Inouye and Kawata 2004a). Due to local four-wave mixing, the tip can emit light with the same frequency as the CARS signal. In addition, after multi-photon excitation, noble metals show white light photoluminescence, which can contribute to the detected signal. Nevertheless, the capability of TE-CARS for spectrally resolved imaging of biopolymers has been demonstrated successfully.

In addition to nanoclusters, DNA was analyzed in form of network structures (Ichimura, Hayazawa, Hashimoto, Inouye and Kawata 2004a). In this case, a solution of poly(dA-dT)-poly(dA-dT) was mixed with a Mg^{2+} solution and subsequently cast and dried on a coverslip. Here, the Mg^{2+} acts as a linker between DNA and negatively charged oxygen atoms of the glass surface.

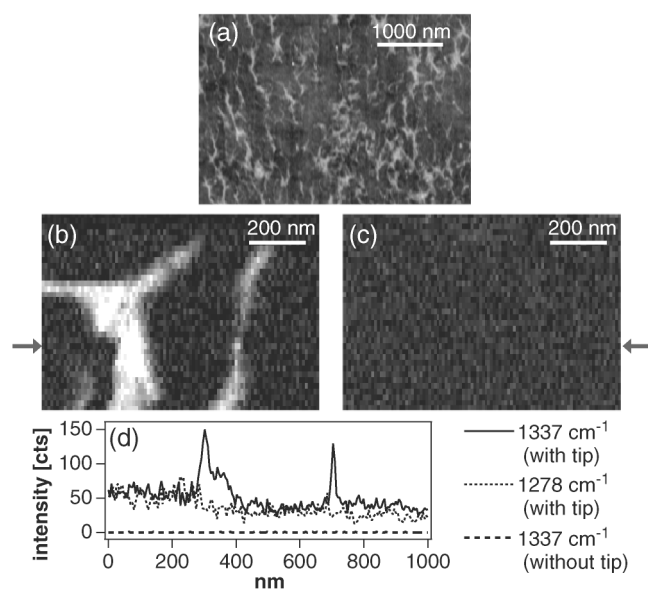


Fig. 6: TE-CARS imaging of the DNA network. (a) Topographic AFM image, (b) TE-CARS image at on-resonant frequency of adenine (1337 cm^{-1}), (c) TE-CARS image at off-resonant frequency (1278 cm^{-1}) and (d) cross sections along the line indicated by the arrows. Reprinted figure with permission from (Ichimura, Hayazawa, Hashimoto, Inouye and Kawata 2004a). Copyright (2004), by the American Physical Society.

The AFM topography image reveals a network consisting of single DNA strands as well as bundles of up to ten DNA molecules (see Fig. 6 (a)). The height of the structures is $\sim 2.5\text{ nm}$ corresponding to the diameter of a single DNA double helix, whereas the width of the bundles varies between 2.5 nm and a few tens of nanometers. TE-CARS images obtained at the on-resonant and off-resonant frequency are shown in Fig. 6 (b) and Fig. 6 (c), respectively. Again, the on-resonant image differs clearly from the corresponding off-resonant image, which can also be seen in the line profiles in Fig. 6 (d). Thus, the on-resonant image is based on a spectroscopic contrast, which allows the imaging of adenine-containing parts of the DNA sample. The active volume in these TE-CARS experiments was estimated to have a diameter of 20 nm and a height of 2.5 nm , which corresponds to the thickness of the sample. Taking into account this volume of approximately one zeptoliter, the estimated enhancement factor is ~ 100 . Determination of the signal-to-noise ratio led to a smallest detectable DNA volume of $\sim 1/4$ zeptoliter. Thus, TE-CARS is a powerful tool for

spectroscopically resolved imaging of biopolymer networks in their native state at the nanometer scale and provides vibrational spectral information from a subzeptoliter volume.

Similarly to TE-CARS, scattering SNOM (s-SNOM) in the IR range provides spectroscopically resolved imaging of DNA networks beyond the diffraction limit (Akhremitchev, Sun, Stebounova and Walker 2002). Nanometer scale imaging based on chemical contrast was demonstrated using patterned samples consisting of alternating areas coated with DNA and 1-hexadecanethiol, respectively. Therefore, monolayers of the two compounds were prepared in the form of 5- μm -wide stripes on gold-coated glass surfaces. Subsequently, 20 μm \times 20 μm areas of the sample surface were scanned by a platinum-coated non-contact AFM tip. For s-SNOM measurements, the tip was side-irradiated by IR radiation from a tunable CO₂ laser with an $\sim 80^\circ$ angle of incidence. The radiation scattered at the tip-sample interface was collected in the same direction and detected by means of a mercury cadmium telluride (MCT) detector.

For s-SNOM imaging of DNA, the excitation wavenumber was tuned to the phosphate absorption band of DNA that is $\omega = 980 \text{ cm}^{-1}$. In this way, DNA-coated areas of the sample could be clearly distinguished from hexadecanethiol stripes, whereas any significant contrast between these regions was visible in the corresponding topography image. The lateral resolution in the s-SNOM measurements was estimated to be around 200 nm by evaluating the signal behavior at the DNA-hexadecanethiol interface. With a sample thickness of $\sim 2.5 \text{ nm}$, the sampled volume is ~ 100 zeptoliter, which is 100 times larger than in the TERS experiments mentioned above. Nevertheless, IR absorption signals from only $\sim 5 \times 10^5$ or approximately one attomol phosphate groups were detected successfully and allowed to distinguish DNA from hexadecanethiol with a lateral resolution of $\sim \lambda/50$.

5.2. Viruses and Biological Tissues

First apertureless near-field optical spectroscopic measurements on biological material were performed using resonant optical scattering spectroscopy (REOSS) (Martin, Zenhausern and Wickramasinghe 1996). Even though the measurements were not based on IR or Raman spectroscopy, this work should be mentioned here because it paved the way for vibrational spectroscopy and imaging of biological samples at the nanometer scale. In REOSS, a sharp AFM tip oscillates in non-contact mode close to the sample surface. Tip and sample are illuminated in transmission mode under total internal reflection. Laser beams having wavelengths of 633 and 514 nm, respectively, were employed for excitation. The system provided a lateral resolution superior to 5 nm.

The tobacco mosaic virus (TMV) was stained using coomassie blue and adsorbed onto cleaved mica. The sample was imaged using non-contact AFM and REOSS. While scanning the sample, both resonant scattering of light and the variation of the tip height with respect to the laser focus affect the REOSS signal. The latter unwanted “liftoff” contribution could be corrected successfully using the independently determined AFM topography data. In this way, both techniques clearly revealed the cylindrical shape of the viruses. A comparison of REOSS measurements at two different wavelengths showed clear evidence for spectroscopic information achievable by this technique. The optical response at 633 nm was almost an order of magnitude stronger than at 514 nm, which is in good agreement with spectroscopic properties of coomassie blue. This result is very promising for further applications of apertureless near-field vibrational spectroscopic methods, i.e. IR and Raman spectroscopy, which should provide nanometer-scale imaging of biological samples without the need of staining.

The first demonstration of apertureless near-field Raman spectroscopy of an intact biological tissue was the application of TERS to the investigation of insect eye surfaces (Anderson and Gaimari 2003). The compound eye of insects consists of hundreds of unit eyes

called ommatidia. The ommatidial lens surfaces in several species of the order Diptera (flies) and the related order Mecoptera were imaged by AFM. The compound eye surfaces in most species under investigation showed a cerebral cortex-like pattern over the entire surface of each individual lens. Cross-sections of the ommatidium of *Chrysopilus testaceipes* revealed periodic height variations of ~ 20 nm with a lateral distance of ~ 190 nm between ridges (see Fig. 7).

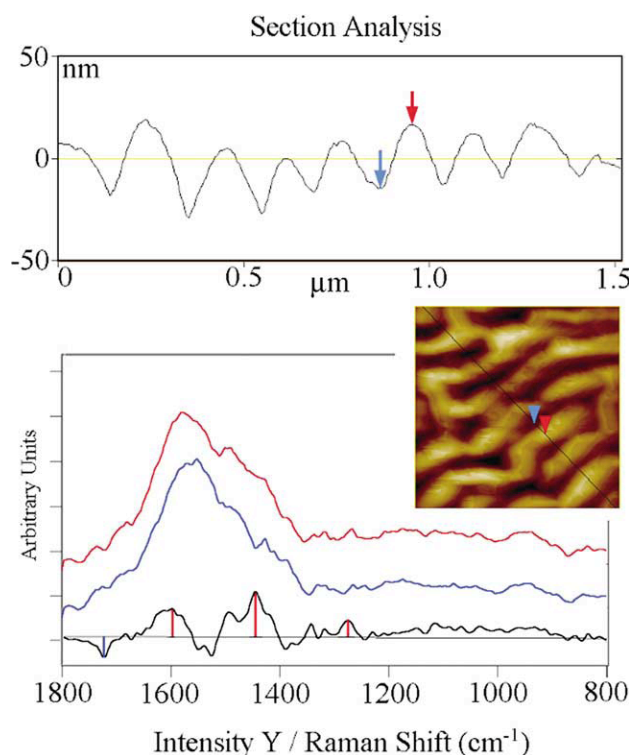


Fig. 7: TERS analysis of the ommatidial lens surface of a *Chrysopilus testaceipes* compound eye. Cross section of the ommatidium (upper graph), AFM phase image (insert), and Raman spectra (lower graph) taken from the top of a ridge (top curve, bottom panel) and the bottom of a trough (middle curve, bottom panel). The bottom curve in the lower graph is the subtraction of the trough spectrum from the ridge spectrum (2× enlarged). Reprinted from (Anderson and Gaimari 2003), with permission from Elsevier.

AFM phase contrast imaging demonstrated variations in chemical composition between ridge and trough, which could be confirmed by TERS measurements. After acquisition of the AFM image, the metallized tip was parked on a ridge and a trough, respectively. Side illumination ($\lambda = 785$ nm) using a microscope objective with an angle of $\sim 87^\circ$ between laser

beam and tip axis and detection through the same objective resulted in two Raman spectra having differences in spectral regions which are characteristic for aliphatic hydrocarbons ($1,465\text{ cm}^{-1}$), carboxylic acids ($1,409\text{ cm}^{-1}$; 1425 cm^{-1}), esters ($1,730\text{ cm}^{-1}$), and proteins ($1,658\text{--}1,672\text{ cm}^{-1}$; $1,310\text{ cm}^{-1}$). The ridges show more peptide bond functionality, whereas in troughs the content of fatty acid esters is increased. The control of surface wetting or anti-reflection coating are possible explanations for the morphological and chemical heterogeneities. This work showed the potential of TERS in the collection of phylogenetic data for a better understanding of evolutionary processes and in applications to biological tissues in general.

6. Applications in Materials Science

6.1. Nanotubes

Single-walled carbon nanotubes (SWNT) was discovered by Iijima in 1991 (Iijima 1991, Iijima and Ichihashi 1993) and have generated intense interest due to their potential applications in nanotechnology. Numerous TERS investigations of SWNTs have been conducted since the near-field Raman imaging of an isolated semi-conducting SWNT by Novotny and co-workers, using an electrochemically etched Ag tip (Anderson, Hartschuh, Cronin and Novotny 2005, Hartschuh, Sanchez, Xie and Novotny 2003, Hayazawa, Yano, Watanabe, Inouye and Kawata 2003, Saito, Hayazawa, Kataura, Murakami, Tsukagoshi, Inouye and Kawata 2005, Wang, Saito, Batchelder, Kirkham, Robinson and Smith 2005). Four Raman modes were observed in that significant work, the radial breathing mode (RBM), two graphitic bands (G, G'), and the disordered (D) band. Strong evidence that an isolated SWNT was detected instead of a bundle comes from the narrow full-width at half maximum (FWHM) of the Raman bands.

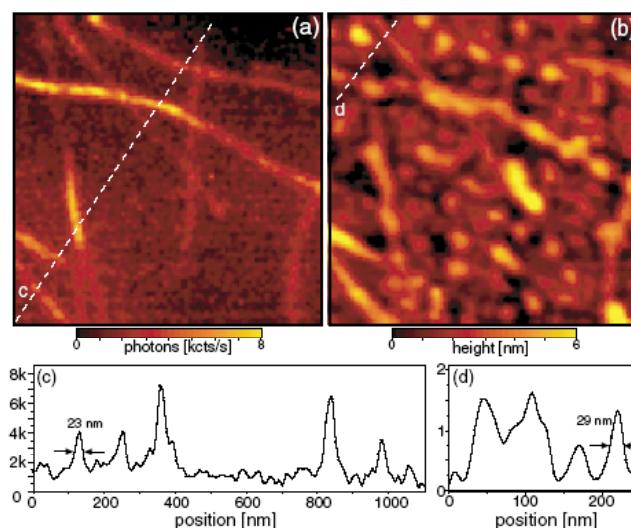


Fig. 8: (a) Near-field Raman image and (b) topographic image of SWNTs dispersed on glass. (c) and (d) Cross-section taken along the dashed line in the Raman and topographic image. Reprinted figure with permission from (Hartschuh, Sanchez, Xie and Novotny 2003). Copyright (2003) by the American Physical Society.

An interesting feature of the experiment is that the near-field resolution (23 nm) is superior to that obtained in the simultaneously-collected topographical image (29 nm). A similar experiment using a Si AFM tip functionalized with an 80 nm Ag particle has revealed that a high spatial resolution of 24 nm can be obtained (Wang, Saito, Batchelder, Kirkham, Robinson and Smith 2005). The near-field enhancement originating from an area much smaller than the size of the scattering particle is consistent with recent finite difference time domain (FDTD) simulations works by Richards and co-workers where at resonance, an optical confinement far sharper than the tip radius has been predicted (Demming, Festy and Richards 2005).

Defect-density imaging has also been demonstrated for an isolated SWNT produced by the arc discharge method (Anderson, Hartschuh, Cronin and Novotny 2005). Bumps of 5 nm in height have been observed on top of the SWNT in the topography image, and these have been assigned to Ni/Y catalyst particles. When localized TERS measurements were performed on spots of the SWNT close to or on the Ni/Y catalyst, the frequencies and intensities of the G and G' bands changed. Differences in the local tube structure, which may

be due to defects, junctions or interactions with the glass substrate may also be revealed from the TERS variation of the RBM frequency (diameter sensitive) and intensity.

The RBM and G-band of SWNTs have been found to exhibit opposite polarization dependences (Saito, Hayazawa, Kataura, Murakami, Tsukagoshi, Inouye and Kawata 2005). The RBM and G bands exhibits greater TERS enhancement with p and s-polarization, respectively. In addition, several symmetry components in the G-band show different enhancement efficiencies, which allow symmetry assignments to be made in the nanometer scale.

Recently, Hartschuh *et al.* presented the first simultaneous near-field photoluminescence and Raman imaging of isolated SWNTs with a spatial resolution better than 15 nm (Hartschuh, Qian, Meixner, Anderson and Novotny 2005). Highly localized and intense photoluminescence was observed from certain sections (20-30 nm) of an arc-discharge produced SWNT and has been assigned to the presence of localized excited states. These states may originate from localized chirality variations occurring from defects or from local environmental perturbations. However, for micelle-encapsulated SWNTs, the photoluminescence emission extends along the tube length (several hundreds of nm). By acquiring simultaneous near-field Raman and photoluminescence images, it is desired that a correlation between structural defects and the photoluminescence properties of individual SWNTs be obtained. More detailed information on carbon nanotube spectroscopy is available in chapter 3 of this volume.

6.2. Material-specific Mapping

Imaging with material-specific spectral contrast using local field enhancement by sharp metal tips can be done with excellent spatial resolution and relatively rapidly, as no spectral scanning or dispersion in a spectrometer is needed. This has been demonstrated for

recognition of components in polymer blends, metal-dielectric composites, and on silicon surfaces.

Polymer blends are a very interesting and promising area of application for TERS and s-SNOM. These blends often show segregation of the polymer phases, forming domains with sizes in the 100 nm range and below. Fillers such as small silica or graphite particles and other additives add to the complexity of such samples, especially materials of industrial relevance. State-of-the-art Raman microspectrometry has a spatial resolution on the order of 1 μm , and is thus not capable to resolve polymer phase domains or filler particles (Zerda, Song and Waddell 2003).

The group of Keilmann has applied IR s-SNOM at fixed wavelengths to image polymer mixtures, polymer films, and polymer beads with excellent spatial resolution. Several reviews about their work have recently appeared (Keilmann 2002, Keilmann 2004, Keilmann and Hillenbrand 2004). The imaging is usually based on a theoretical calculation of the near-field extinction or scattering efficiency as a function of incident photon energy of the materials to be studied (Hillenbrand, Taubner and Keilmann 2002). A suitable wavelength is then chosen that gives maximum contrast between the compounds present on the sample surface, and s-SNOM images are recorded, often using double modulation methods (Taubner, Hillenbrand and Keilmann 2003). High contrast can be achieved between metals and high-refractive index dielectric compounds (Knoll and Keilmann 1999), and a spatial resolution of less than 10 nm has been found (Hillenbrand and Keilmann 2002) even at IR wavelengths of $\lambda \approx 10 \mu\text{m}$, corresponding to a resolution of $\lambda/1000$. While the contrast is material dependent, the spatial resolution is not, but is determined by the properties of the tip alone. It is somewhat misleading, though, to talk about “spectroscopic imaging” and “identification” of materials in this context. While an image at fixed wavelength can be recorded in a few minutes (for the sake of argument, we assume 5 min), true spectroscopic imaging would take much longer. If a spectral range of $\Delta\omega = 2000 \text{ cm}^{-1}$ should be covered with a resolution of

10 cm^{-1} , 200 scans would be necessary, requiring a total of 1000 minutes, i.e., over 16 hours. This is problematic due to long-term drifts of STM and AFM equipment. Suitable laser sources that are continuously tunable through the IR are also not readily available.

Fig. 9 shows the imaging of a PMMA / PS polymer blend with a resolution of $< 70\text{ nm}$ carried out at different IR wavelengths in the $5.5\text{ to }6\text{ }\mu\text{m}$ range (Taubner, Hillenbrand and Keilmann 2004). This example demonstrates very nicely how spectroscopic contrast is achieved at an appropriate (fixed) wavelength, and how the contrast is completely reversed at another wavelength.

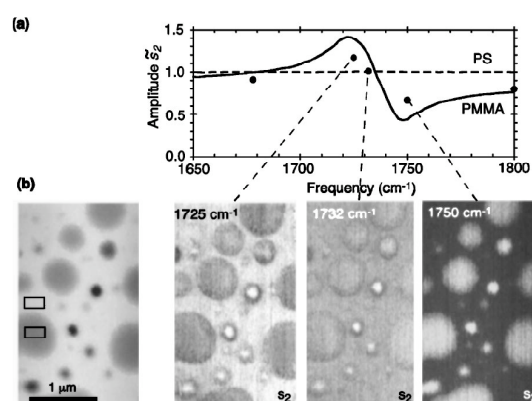


Fig. 9: s-SNOM analysis of PS in a PMMA matrix. (a) calculated s-SNOM amplitude spectra of PMMA (solid line) and of PS (dashed line). (b) topography (left) and IR amplitude (right) s-SNOM images of a 70 nm thick polymer blend film on Si at three different frequencies, as indicated in (a). The extracted IR contrast of PMMA relative to PS obtained by averaging in the regions indicated in the topography is shown as experimental data points in (a). Reprinted from (Taubner, Hillenbrand and Keilmann 2004)}, with permission of the American Institute of Physics.

An interesting method was developed by these authors to prepare topographically flat polymer composite samples. Immiscible polymers, for example polystyrene (PS) and polymethylmethacrylate (PMMA) were sequentially dried on cleaved NaCl, followed by dissolving the NaCl in water. This yielded a nearly flat polymer surface with sharp material boundaries (Knoll and Keilmann 1999). The same experimental approach can be used to study other materials. For example, Keilmann and coworkers have shown examples ranging

from SiC partially covered with Au (Hillenbrand, Taubner and Keilmann 2002) to metal / Si / polymer three-component samples (Taubner, Hillenbrand and Keilmann 2003).

Anderson demonstrated the feasibility of combining IR photoacoustic spectroscopy with AFM detection (Anderson 2000a). Chopped radiation from an IR spectrometer was focused on the sample surface and surface deflections caused by photoacoustic pressure waves were detected by means of an AFM cantilever. The frequency of the generated acoustic waves equals to the chopper frequency that was 3 to 4 Hz in this case. The ability to determine material-dependent signals from an area having a diameter of ~ 100 nm allowed the discrimination between fluorinated ethylene propylene (FEP) copolymer and polystyrene. The main advantage of photoacoustic detection compared to conventional s-SNOM lies in its capability of depth-resolved measurements and the detection of subsurface structures. Multi-layered samples consisting of Cr on SiO₂ or Cr and Al on SiO₂ were irradiated by chopped IR radiation (Tomoda, Shiraishi, Kolosov and Wright 2003). Since the chopper frequency was in the MHz range, ultrasonic waves were generated by the photoacoustic effect. For detection, ultrasound was converted into kHz waves by interference between photoacoustic waves and vibrations of the cantilever at a slightly shifted frequency. The authors called this “optical heterodyne force microscopy” (OHFM). A material-specific contrast with a lateral resolution of ~ 50 nm could be obtained, even in the case of buried structures, although data interpretation remains somewhat difficult.

6.3. Semiconductors

The possibility to conduct nanoscale stress mapping of silicon transistors has been gaining importance because of performance issues created by mechanical stress from miniaturization of these devices. The frequency, bandwidths and band shapes of the phonon Raman bands are sensitive to the presence of stress, strains and impurities.

Silicon surfaces have been studied by Sun and Shen (Sun and Shen 2001, Sun, Shen, Cheong, Yu, Lim and Lin 2002, Sun and Shen 2003a, 2003b). Near-field Raman mapping of a Si device consisting of 380 nm wide SiO₂ lines separated by 300 nm has been performed. 100 nm pitches in Si that was oxidized by thermal annealing have also been investigated with TERS using an Ag coated quartz AFM tip (Poborchii, Tada and Kanayama 2005). The Si-Si stretching frequency has been found to increase at the proximity of the pitch. This demonstrates that compression at the Si/SiO₂ boundary between the pitch and the rest of the substrate has occurred during the thermal oxidation process.

Lahrech *et al.* have demonstrated successfully that implanted boron lines in silicon can be detected by IR s-SNOM even in the absence of any topographical contrast (Lahrech, Bachelot, Gleyzes and Boccara 1997). The setup was based on side irradiation of an oscillating tungsten tip by means of a CO₂ laser and provided lateral resolution of ~ 400 nm. Knoll and Keilmann have also performed near-field IR measurements on doped Si and have shown that subsurface mobile carriers can be probed by their response to an IR near-field with a yet-to-be fully optimized spatial resolution of 30 nm (Knoll and Keilmann 2000).

Micro-SERS has been performed on Si_{1-x}Ge_x for highly sensitive detection of the surface of strained Si using an epi-illuminescence setup (Hayazawa, Motohashi, Saito and Kawata 2005). A strained 30-nm-thick Si layer is grown on a Ge-doped Si substrate, and this side is placed facing the high NA objective and illuminated. A small shoulder at 513.8 cm⁻¹ is observed and attributed to the strained Si. When a similar substrate is covered with a 10-nm fractal-like Ag film, this signal is shifted to 515.3 cm⁻¹. This blue-shift is attributed to the presence of neighboring Ag atoms. Thus, the supposedly Raman-enhancing Ag layer affects the result of the analysis. This experiment has been suggested as a precursor for TERS using a sharpened metallized cantilever tip with side-on illumination. A better spatial resolution should be achievable. We suggest that for experiments of this nature, metallized silica fiber tips based on a tuning fork feedback or etched metal wires and STM feedback are better

alternatives for two reasons. The first is to avoid perturbation from chemical bonding or pressure effects when the tip is in contact with the Si sample (Watanabe, Ishida, Hayazawa, Inouye and Kawata 2004). The second is of a practical nature since the Si AFM tip would give very similar Raman signals that may interfere with the analysis of the strained Si bands.

Subsurface defects in semiconductors can also be detected by combinations of SPM techniques and photoacoustic spectroscopy (Hida, Mera and Maeda 2001). Chopped near-IR irradiation of GaAs semiconductors and detection of photoacoustic waves using an STM allowed the imaging of subsurface defect structures with nanometer resolution. The imaging contrast was in good agreement with the spectroscopic properties of defect and non-defect sites.

6.4. SERS Substrates

Apertureless near-field optical microscopy is also a tool for investigating surface plasmon resonances, which provide the basis for both, SERS and TERS. While light intensity distributions on irradiated SERS substrates can be determined in aperture SNOM experiments (Klar, Perner, Grosse, von Plessen, Spirkl and Feldmann 1998, Krenn, Dereux, Weeber, Bourillot, Lacroute, Goudonnet, Schider, Gotschy, Leitner, Aussenegg and Girard 1999, Krenn, Weeber, Dereux, Bourillot, Goudonnet, Schider, Leitner, Aussenegg and Girard 1999), apertureless s-SNOM techniques allow the measurement of local electric field enhancements with nanometer resolution (Adam, Benrezzak, Bijeon and Royer 2000, Hillenbrand and Keilmann 2001, Hillenbrand, Keilmann, Hanarp, Sutherland and Aizpurua 2003). An s-SNOM setup based on an AFM operated in tapping mode and side illumination of the tip with visible laser radiation was applied to investigate surface plasmons on single isolated gold nanospheres (Adam, Benrezzak, Bijeon and Royer 2000). By tuning the

excitation wavelength, plasmon resonance spectra of individual particles could be determined.

A screening of nanoparticles with regard to their SERS activity can be performed by scanning immobilized particles even in close aggregations at a fixed wavelength. Whereas the topography image reveals the whole aggregate, in the optical near-field amplitude image only the particles are visible which at least partially fulfill the resonance condition at the excitation wavelength under investigation with respect to size, shape, and orientation. This could be demonstrated successfully by the group of Keilmann by use of their s-SNOM setup with 633 nm side illumination and PtIr coated Si tips (Hillenbrand and Keilmann 2001). In addition to the signal amplitude mentioned above, evaluation of the phase signal enables the elucidation of the plasmon modes that are excited. Gap mode plasmons between densely packed gold nanoparticles could be found by scanning particle aggregates with sharper uncoated Si probes. Although gap mode plasmons were clearly visible in the s-SNOM images, the highest field enhancements are expected to be deeper inside the particle aggregates and are therefore not accessible to the tip. A possibility to solve this problem can be the use of carbon nanotubes attached to a conventional AFM probe. Such a supertip was applied to the visualization of surface plasmons on disk-shaped gold islands on a glass surface (Hillenbrand, Keilmann, Hanarp, Sutherland and Aizpurua 2003). A bundle of carbon nanotubes on an AFM probe resulted in a tip radius of ~ 25 nm, a value that could probably be improved down to a few nanometers by use of single-walled carbon nanotubes. Highly resolved s-SNOM images of the disks having a diameter of 91 nm resulted in a reproducible pattern consisting of two bright areas separated by a narrow dark zone showing evidence for a dipolar plasmon oscillation. Although the gold disk structures could be fabricated with good reproducibility, highly significant differences in the optical amplitude image between individual gold islands were observed. This finding was explained by shifts of the resonance

frequency and underlined the strong dependence of surface plasmon resonances on small changes in size, shape, and environment of each particle.

The techniques described in this section can help to systematically investigate parameters that influence surface plasmon resonances and to better understand SERS and related effects. Thus, they can be useful tools in the improvement of SERS substrates as well as in the screening of nanoparticles that are potential probes for TERS experiments.

7. Conclusions and Outlook

We presented the use of tip-enhanced vibrational spectroscopy for the investigation of biological objects, nanostructured materials, and for the observation of highly localized chemical processes. The technology has not yet reached a state where routine nanoscale chemical analysis can be performed. This is evident from the scarcity of literature demonstrating applications to real-life problems. However, the technology is maturing, and we are confident that TERS and related methodologies have excellent potential for nanoscale molecular identification and spectroscopy.

Tens of different near-field vibrational spectroscopy and microscopy investigations have been published over the last 10 years. We like to make some general comments about these techniques to aid the reader in assessing their practical usefulness. From the point of view of nanoscale chemical analysis, the issues of spatial resolution, sensitivity and selectivity are important. For practical reason, instrumental complexity and price are also considered. According to these criteria, TERS is probably the best choice. The setup is easy to build: it is only necessary to combine a Raman microscope and a SPM instrument, both of which have been commercially available for more than 10 years. The best spatial resolution of TERS is around 10-20 nm (Anderson, Hartschuh, Cronin and Novotny 2005) and the

sensitivity is high enough to investigate the Raman spectrum from tens of molecules (Pettinger, Ren, Picardi, Schuster and Ertl 2004). In our opinion, TERS has the potential to detect Raman scattering from single molecules under optimum conditions. Near-field IR microscopy has also been very successful. For example, it allows to distinguish different polymer phases with a spatial resolution of 10 nm (Hillenbrand, Taubner and Keilmann 2002), which is slightly better than TERS. On the other hand, its drawbacks are obvious: real spectra are difficult to record due to the need to tune a laser through the IR spectral range. White light sources have also been combined with SPM and FTIR (Narita and Kimura 2001), but both, signal-to-noise ratio and spatial resolution were poor because of the absence of a mechanism to enhance the near-field signal. Furthermore, from a practical view, there is no commercial instrument yet that can be used directly for near-field IR microscopy, perhaps because handling IR radiation is more difficult than visible light. Other s-SNOM methods also succeeded to a certain extent. The main problem of s-SNOM methods is that their chemical selectivity is poor compared to methods based on true vibrational spectroscopy, limiting their application to analytical and bioanalytical chemistry.

A key issue when employing tip-enhanced vibrational spectroscopy is that the near-field signal intensity that can be obtained is small, because it originates from a very small area and is easily overwhelmed by background from the total illuminated area. Ways to overcome this difficulty, and to develop TERS into a robust method have therefore received much attention in this chapter. A high enhancement factor not only implies greater signal, but greater near-field to far-field contrast. A large contrast will eliminate the need to perform background subtraction and will ultimately permit a reasonable imaging speed.

Methods for estimating or calculating enhancement factors have to be carefully selected based on the type of sample (e.g. its thickness and uniformity). A comparison of different enhancement factors is only possible if the parameters of the calculation are well defined and precisely known. In our opinion, the near-field to far-field contrast is a more useful quantity

for comparison, and is also of greater practical relevance than the enhancement factor. The contrast can be improved by optimizing the near-field enhancement (annular illumination, optimized polarization to increase the p-component, excitation by a tunable laser to hit the plasmon resonance), by suppressing the far-field background (high NA epi-illumination, annular illumination, far-field suppression by use of appropriate polarization geometry), or generally by the best possible compromise between both strategies.

The highest enhancement factors that have been reported to date are in the 10^6 range, the highest TERS contrast is $\sim 10,000$. The best lateral resolution achieved with these methods is on the order of 10-20 nm for TERS, 17 nm for IR s-SNOM, and 10 nm down to 1 nm for Vis s-SNOM. The main fields of application that are described in this chapter, are dyes, catalysis, biopolymers and biological samples, SWNTs, material-specific mapping, and semiconductors.

Finally, we would like to point out that vibrational spectroscopy is not the only method to gain detailed analytical chemical information on a lateral scale of nanometers. Near-field ultrasound measurements with high spatial resolution afforded by the presence of an AFM probe have started to appear in the literature (Blodgett and Spicer 1999, Inagaki, Kolosov, Briggs and Wright 2000, Moreau and Ketterson 1992, Shekhawat and Dravid 2005, Yamanaka, Ogiso and Kolosov 1994). In the future, related imaging methods with high spatial resolution and chemical contrast may become feasible. Several research groups have presented very interesting work on near-field or tip-enhanced laser surface melting and laser ablation (Boneberg, Munzer, Tresp, Ochmann and Leiderer 1998, Chimmalgi, Choi, Grigoropoulos and Komvopoulos 2003, Chimmalgi, Grigoropoulos and Komvopoulos 2005, Chimmalgi, Hwang and Grigoropoulos 2005, Dickmann, Jersch and Demming 1997, Huang, Hong, Lu, Lukyanchuk, Song and Chong 2002, Huber, Koch and Feldmann 1998, Jersch and Dickmann 1996, Jersch, Demming and Dickman 1997, Lu, Mai, Qiu and Chim 1999). The interfacing of such methods with mass spectrometric detection of the ablation products is an

equally fascinating prospect (Kossakowski, O'Connor, Widmer, Baldeshwieler and Beauchamp 1998, Stöckle, Setz, Deckert, Lippert, Wokaun and Zenobi 2001).

8. Acknowledgements

We thank M.S. Anderson, Y. Inouye, F. Keilmann, R. Martinez, and L. Novotny for providing original figures for this chapter. Financial support for our work from the Deutsche Forschungsgemeinschaft (to TS), the ETH Zurich, and the Gebert Rüt Stiftung is greatly appreciated.

9. References

- Adam, P.M., S. Benrezzak, J.L. Bijeon, P. Royer, 2000, *J. Appl. Phys.* 88, 6919.
- Akhremitchev, B.B., Y.J. Sun, L. Stebounova, G.C. Walker, 2002, *Langmuir* 18, 5325.
- Anderson, M.S., 2000a, *Appl. Spectrosc.* 54, 349.
- Anderson, M.S., 2000b, *Appl. Phys. Lett.* 76, 3130.
- Anderson, M.S., W.T. Pike, 2002, *Rev. Sci. Instrum.* 73, 1198.
- Anderson, M.S., S.D. Gaimari, 2003, *J. Struct. Biol.* 142, 364.
- Anderson, M.S., 2005, *Anal. Chem.* 77, 2907.
- Anderson, N., A. Hartschuh, S. Cronin, L. Novotny, 2005, *J. Am. Chem. Soc.* 127, 2533.
- Aravind, P.K., H. Metiu, 1983, *Surf. Sci.* 124, 506.
- Atesang, J., R. Geer, 2005, *Proc. SPIE* 5766, 134.
- Barbara, A., T. Lopez-Rios, P. Quemerais, 2005, *Rev. Sci. Instrum.* 76, 023704.
- Blodgett, D.W., J.B. Spicer, 1999, *Appl. Phys. Lett.* 74, 3735.
- Boneberg, J., H.J. Munzer, M. Tresp, M. Ochmann, P. Leiderer, 1998, *Appl. Phys. A* 67, 381.
- Bulgarevich, D.S., M. Futamata, 2004, *Appl. Spectrosc.* 58, 757.

Chimmalgi, A., T.Y. Choi, C.P. Grigoropoulos, K. Komvopoulos, 2003, *Appl. Phys. Lett.* 82, 1146.

Chimmalgi, A., C.P. Grigoropoulos, K. Komvopoulos, 2005, *J. Appl. Phys.* 97, 104319.

Chimmalgi, A., D.J. Hwang, C.P. Grigoropoulos, 2005, *Nano Lett.* 5, 1924.

Clicq, D., S. Vankrunkelsven, W. Ranson, C. De Tandt, G.V. Barn, G. Desmet, 2004, *Anal. Chim. Act.* 507, 79.

Cremer, P.S., X.C. Su, G.A. Somorjai, Y.R. Shen, 1998, *J. Mol. Catal. A* 131, 225.

Demming, A.L., F. Festy, D. Richards, 2005, *J. Chem. Phys.* 122, 184716.

Dickmann, K., J. Jersch, F. Demming, 1997, *Surf. Interface Anal.* 25, 500.

Fokas, C., V. Deckert, 2002, *Appl. Spectrosc.* 56, 192.

Hartschuh, A., N. Anderson, L. Novotny, 2003, *J. Microsc.-Oxford* 210, 234.

Hartschuh, A., E.J. Sanchez, X.S. Xie, L. Novotny, 2003, *Phys. Rev. Lett.* 90, 095503.

Hartschuh, A., H. Qian, A.J. Meixner, N. Anderson, L. Novotny, 2005, *Nano Lett.* 5, 2310.

Hayazawa, N., Y. Inouye, Z. Sekkat, S. Kawata, 2000, *Opt. Commun.* 183, 333.

Hayazawa, N., Y. Inouye, Z. Sekkat, S. Kawata, 2001, *Chem. Phys. Lett.* 335, 369.

Hayazawa, N., Y. Inouye, Z. Sekkat, S. Kawata, 2002, *J. Chem. Phys.* 117, 1296.

Hayazawa, N., A. Tarun, Y. Inouye, S. Kawata, 2002, *J. Appl. Phys.* 92, 6983.

Hayazawa, N., T. Yano, H. Watanabe, Y. Inouye, S. Kawata, 2003, *Chem. Phys. Lett.* 376, 174.

Hayazawa, N., T. Ichimura, M. Hashimoto, Y. Inouye, S. Kawata, 2004, *J. Appl. Phys.* 95, 2676.

Hayazawa, N., M. Motohashi, Y. Saito, S. Kawata, 2005, *Appl. Phys. Lett.* 86, 263114.

Hida, A., Y. Mera, K. Maeda, 2001, *Appl. Phys. Lett.* 78, 3190.

Hillenbrand, R., F. Keilmann, 2000, *Phys. Rev. Lett.* 85, 3029.

Hillenbrand, R., F. Keilmann, 2001, *Appl. Phys. B* 73, 239.

Hillenbrand, R., F. Keilmann, 2002, *Appl. Phys. Lett.* 80, 25.

Hillenbrand, R., T. Taubner, F. Keilmann, 2002, *Nature* 418, 159.

Hillenbrand, R., F. Keilmann, P. Hanarp, D.S. Sutherland, J. Aizpurua, 2003, *Appl. Phys. Lett.* 83, 368.

Huang, S.M., M.H. Hong, Y.F. Lu, B.S. Lukyanchuk, W.D. Song, T.C. Chong, 2002, *J. Appl. Phys.* 91, 3268.

Huber, R., M. Koch, J. Feldmann, 1998, *Appl. Phys. Lett.* 73, 2521.

Ichimura, T., N. Hayazawa, M. Hashimoto, Y. Inouye, S. Kawata, 2003, *J. Raman Spectrosc.* 34, 651.

Ichimura, T., N. Hayazawa, M. Hashimoto, Y. Inouye, S. Kawata, 2004a, *Phys. Rev. Lett.* 92, 220801.

Ichimura, T., N. Hayazawa, M. Hashimoto, Y. Inouye, S. Kawata, 2004b, *Appl. Phys. Lett.* 84, 1768.

Iijima, S., 1991, *Nature* 354, 56.

Iijima, S., T. Ichihashi, 1993, *Nature* 363, 603.

Inagaki, K., O.V. Kolosov, G.A.D. Briggs, O.B. Wright, 2000, *Appl. Phys. Lett.* 76, 1836.

Jersch, J., K. Dickmann, 1996, *Appl. Phys. Lett.* 68, 868.

Jersch, J., F. Demming, K. Dickman, 1997, *Appl. Phys. A* 64, 29.

Kalkbrenner, T., M. Ramstein, J. Mlynek, V. Sandoghdar, 2001, *J. Microsc.-Oxford* 202, 72.

Keilmann, F., 2002, *Vib. Spectrosc.* 29, 109.

Keilmann, F., 2004, *J. Electron Microsc.* 53, 187.

Keilmann, F., R. Hillenbrand, 2004, *Philos. T. Roy. Soc. A* 362, 787.

Klar, T., M. Perner, S. Grosse, G. von Plessen, W. Spirkl, J. Feldmann, 1998, *Phys. Rev. Lett.* 80, 4249.

Knoll, B., F. Keilmann, 1999, *Nature* 399, 134.

Knoll, B., F. Keilmann, 2000, *Appl. Phys. Lett.* 77, 3980.

Kobayashi, M., K. Fujita, T. Kaneko, T. Takamatsu, O. Nakamura, S. Kawata, 2002, *Opt. Lett.* 27, 1324.

Kossakovski, D., S.D. O'Connor, M. Widmer, J.D. Baldeshwieler, J.L. Beauchamp, 1998, *Ultramicroscopy* 71, 111.

Krenn, J.R., A. Dereux, J.C. Weeber, E. Bourillot, Y. Lacroute, J.P. Goudonnet, G. Schider, W. Gotschy, A. Leitner, F.R. Aussenegg, C. Girard, 1999, *Phys. Rev. Lett.* 82, 2590.

Krenn, J.R., J.C. Weeber, A. Dereux, E. Bourillot, J.P. Goudonnet, B. Schider, A. Leitner, F.R. Aussenegg, C. Girard, 1999, *Phys. Rev. B* 60, 5029.

Lahrech, A., R. Bachelot, P. Gleyzes, A.C. Boccara, 1996, *Opt. Lett.* 21, 1315.

Lahrech, A., R. Bachelot, P. Gleyzes, A.C. Boccara, 1997, *Appl. Phys. Lett.* 71, 575.

Lu, Y.F., Z.H. Mai, G. Qiu, W.K. Chim, 1999, *Appl. Phys. Lett.* 75, 2359.

Martin, Y., F. Zenhausern, H.K. Wickramasinghe, 1996, *Appl. Phys. Lett.* 68, 2475.

Mehtani, D., N. Lee, R.D. Hartschuh, A. Kisliuk, M.D. Foster, A.P. Sokolov, J.F. Maguire, 2005a, *Proc. SPIE* 5927, 592707.

Mehtani, D., N. Lee, R.D. Hartschuh, A. Kisliuk, M.D. Foster, A.P. Sokolov, J.F. Maguire, 2005b, *J. Raman Spectrosc.* 36, 1068.

Mills, D.L., 2002, *Phys. Rev. B* 65, 125419.

Moreau, A., J.B. Ketterson, 1992, *J. Appl. Phys.* 72, 861.

Narita, Y., S. Kimura, 2001, *Anal. Sci.* 17, i685.

Nieman, L.T., G.M. Krampert, R.E. Martinez, 2001, *Rev. Sci. Instrum.* 72, 1691.

Nonnenmacher, M., M.P. Oboyle, H.K. Wickramasinghe, 1991, *Appl. Phys. Lett.* 58, 2921.

Nonnenmacher, M., H.K. Wickramasinghe, 1992, *Ultramicroscopy* 42, 351.

Novotny, L., R.X. Bian, X.S. Xie, 1997, *Phys. Rev. Lett.* 79, 645.

Novotny, L., E.J. Sanchez, X.S. Xie, 1998, *Ultramicroscopy* 71, 21.

Patanè, S., P.G. Gucciardi, M. Labardi, M. Allegrini, 2004, *Riv. Nuovo Cim.* 27, 1.

Pettinger, B., G. Picardi, R. Schuster, G. Ertl, 2003, *J. Electroanal. Chem.* 554, 293.

Pettinger, B., B. Ren, G. Picardi, R. Schuster, G. Ertl, 2004, *Phys. Rev. Lett.* 92, 096101.

Pettinger, B., B. Ren, G. Picardi, R. Schuster, G. Ertl, 2005, *J. Raman Spectrosc.* 36, 541.

Poborchii, V., T. Tada, T. Kanayama, 2005, *Jpn. J. Appl. Phys.* 2 44, L202.

Ren, B., G. Picardi, B. Pettinger, 2004, *Rev. Sci. Instrum.* 75, 837.

Ren, B., G. Picardi, B. Pettinger, R. Schuster, G. Ertl, 2005, *Angew. Chem. Int. Ed.* 44, 139.

Saito, Y., N. Hayazawa, H. Kataura, T. Murakami, K. Tsukagoshi, Y. Inouye, S. Kawata, 2005, *Chem. Phys. Lett.* 410, 136.

Shekhawat, G.S., V.P. Dravid, 2005, *Science* 310, 89.

Somorjai, G.A., G. Rupprechter, 1999, *J. Phys. Chem. B* 103, 1623.

Stokes, D.L., Z.H. Chi, T. Vo-Dinh, 2004, *Appl. Spectrosc.* 58, 292.

Stöckle, R., P. Setz, V. Deckert, T. Lippert, A. Wokaun, R. Zenobi, 2001, *Anal. Chem.* 73, 1399.

Stöckle, R.M., Y.D. Suh, V. Deckert, R. Zenobi, 2000, *Chem. Phys. Lett.* 318, 131.

Sun, W.X., Z.X. Shen, 2001, *Mater. Phys. Mechan.* 4, 17.

Sun, W.X., Z.X. Shen, F.C. Cheong, G.Y. Yu, K.Y. Lim, J.Y. Lin, 2002, *Rev. Sci. Instrum.* 73, 2942.

Sun, W.X., Z.X. Shen, 2003a, *J. Raman Spectrosc.* 34, 668.

Sun, W.X., Z.X. Shen, 2003b, *Ultramicroscopy* 94, 237.

Taubner, T., R. Hillenbrand, F. Keilmann, 2003, *J. Microsc.* 210, 311.

Taubner, T., R. Hillenbrand, F. Keilmann, 2004, *Appl. Phys. Lett.* 85, 5064.

Tian, Z.Q., B. Ren, D.Y. Wu, 2002, *J. Phys. Chem. B* 106, 9463.

Tomoda, M., N. Shiraishi, O.V. Kolosov, O.B. Wright, 2003, *Appl. Phys. Lett.* 82, 622.

Vankrunkelsven, S., D. Clicq, D. Cabooter, W. De Malsche, J.G.E. Gardeniers, G. Desmet, 2006, *J. Chromatogr. A* 1102, 96.

Wang, J.J., D.A. Smith, D.N. Batchelder, Y. Saito, J. Kirkham, C. Robinson, K. Baldwin, G. Li, B. Bennett, 2003, *J. Microsc.-Oxford* 210, 330.

Wang, J.J., Y. Saito, D.N. Batchelder, J. Kirkham, C. Robinson, D.A. Smith, 2005, Appl. Phys. Lett. 86, 263111.

Watanabe, H., Y. Ishida, N. Hayazawa, Y. Inouye, S. Kawata, 2004, Phys. Rev. B 69, 155418.

Weaver, J.M.R., L.M. Walpita, H.K. Wickramasinghe, 1989, Nature 342, 783.

Wessel, J., 1985, J. Opt. Soc. Am. B 2, 1538.

Wu, X., Y. Wang, J. Wang, Q. Tian, J. Yu, 2005, Proc. SPIE 5635, 292.

Yamanaka, K., H. Ogiso, O. Kolosov, 1994, Appl. Phys. Lett. 64, 178.

Zayats, A.V., 1999, Opt. Commun. 161, 156.

Zenhausern, F., Y. Martin, H.K. Wickramasinghe, 1995, Science 269, 1083.

Zerda, T.W., G. Song, W.H. Waddell, 2003, Proc. Spring ACS Rubber Div. Meeting 76, 769.

Zumbusch, A., G.R. Holtom, X.S. Xie, 1999, Phys. Rev. Lett. 82, 4142.